The C6H4(NH3)2(NO3)2 assembly investigations: Crystal structure, optical properties and impedance spectroscopy, electrical relaxation with Ac conductivity studies

N Hannachi, Thierry Roisnel, F Hlel

N Hannachi, Thierry Roisnel, F Hlel. The C6H4(NH3)2(NO3)2 assembly investigations: Crystal structure, optical properties and impedance spectroscopy, electrical relaxation with Ac conductivity studies. Journal of Molecular Structure, 2022, 1253, pp.132193. 10.1016/j.molstruc.2021.132193. hal-03557826

HAL Id: hal-03557826
https://hal.science/hal-03557826v1

Submitted on 4 Feb 2022

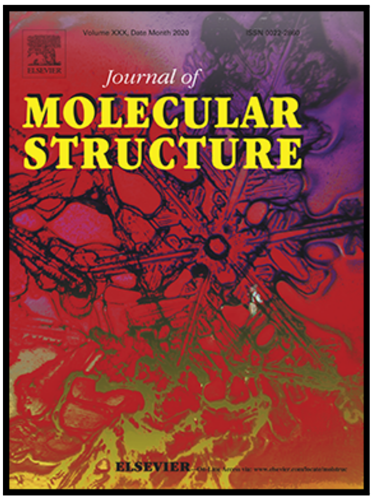

The $C_6H_4(NH_3)_2(NO_3)_2$ assembly investigations: Crystal structure, Optical properties and impedance spectroscopy, electrical relaxation with Ac conductivity studies

N. HANNACHI , T. ROISNEL , F. HLEL

PII: S0022-2860(21)02313-9
DOI: https://doi.org/10.1016/j.molstruc.2021.132193
Reference: MOLSTR 132193

To appear in: *Journal of Molecular Structure*

Received date: 29 October 2021
Revised date: 9 December 2021
Accepted date: 13 December 2021

Please cite this article as: N. HANNACHI , T. ROISNEL , F. HLEL , The $C_6H_4(NH_3)_2(NO_3)_2$ assembly investigations: Crystal structure, Optical properties and impedance spectroscopy, electrical relaxation with Ac conductivity studies, *Journal of Molecular Structure* (2021), doi: https://doi.org/10.1016/j.molstruc.2021.132193

The $C_6H_4(NH_3)_2(NO_3)_2$ assembly investigations : Crystal structure , Optical properties and impedance spectroscopy, electrical relaxation with Ac conductivity studies.

N. HANNACHI [a] ; T. ROISNEL [b] and F. HLEL [a]
[a] Laboratory of spectroscopic characterization and optics of materials, Faculty of Sciences, University of Sfax, B. P. 1171, 3000 Sfax, Tunisia.
[b]Univ Rennes, CNRS, ISCR (Institut des Sciences Chimiques de Rennes) – UMR 6226, F-35000 Rennes, France
.
***Corresponding author:** hnejeh@yahoo.fr

Highlights

- The crystal structure exhibits organic and inorganic layers and alternate along the *c-axis*.
- The 3D Hirshfeld surfaces and the associated 2D fingerprint plots were investigated for intermolecular interactions.
- The vibrational experimental frequencies were also predicted .
- The optical properties were studied by UV–visible absorption spectroscopy
- The electrical and dielectric analysis

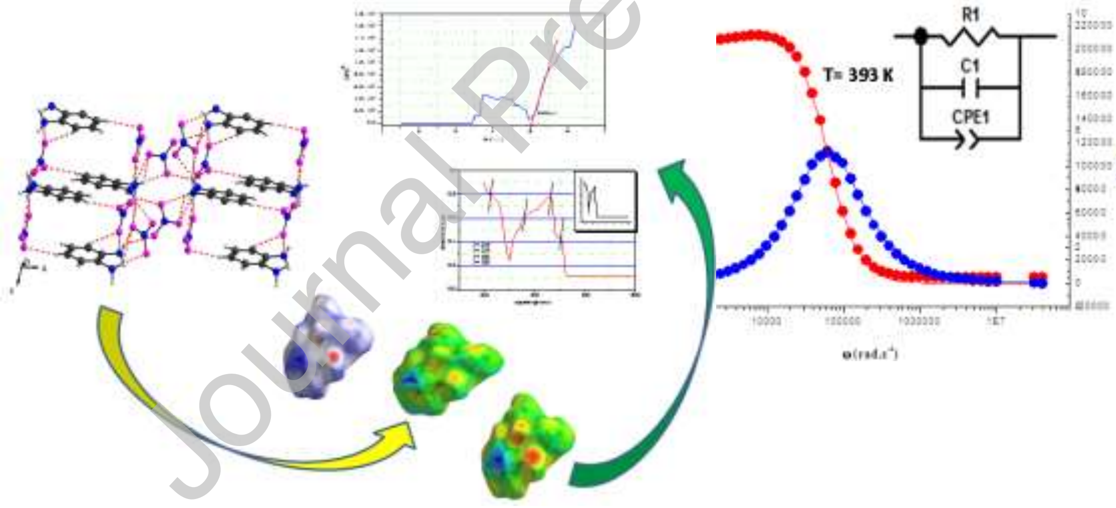

Graphical abstract

Abstract

The assembly involving ($[C_6H_4(NH_3)_2]^{2+}/(NO_3)^-$) hybrid as building units has been conceived to carefully produce hybrid-supramlecules with H- bonded nitrogen, which is expected to replace conventional optical materials. Successfully obtained, a new hybrid compound, $C_6H_4(NH_3)_2(NO_3)_2$ by hydrothermal methods and characterized using single-crystal X-ray diffraction method, Hirshfeld surface analysis, IR / CP MAS- NMR spectroscopy and UV–vis spectrophotometry. Electrical properties and ac conductivity of the title compound has been reported in the temperature and frequency range from 303 to 413 K and 1–10^6 Hz, respectively. The impedance and electrical modulus spectral data and the frequency and temperature correlation analysis of the Nyquist plots has shown that the grains and grain boundaries contribute to the electrical properties of the prepared materials.

The single crystals were obtained by a hydrothermal method. It was found to crystallize in the monoclinic system $P2_1/c$ with the following lattice parameters: a = 12.6966(17) Å; b = 7.9444(11) Å c = 10.3904(14) Å ; β = 105.68(0) and Z = 4. The structural analysis shows that the presence of a layer arrangement perpendicular to the c-axis: planes of $[C_6H_4(NH_3)_2]^{2+}$ cations alternated with planes of two anionic group $(NO_3)^-$ anions. The cohesion of the molecular arrangement is ensured by hydrogen bonding C–H···O and N– H···O. Hirshfeld Surface analysis of intermolecular interactions confirmed that the hydrogen bonds: C/H, H/C, H/O/H/O and H/H contacts, play a dominant role in the crystal structure of the investigated compounds. Infrared and MAS NMR spectroscopic measurements were carried out to confirm the results obtained by X-ray diffraction. In optical studies, data analysis revealed the existence of optical direct with the band gap energy equal to 5.03 eV.

The ac electrical conductivity is investigated at the frequency and temperature. The two semicircles observed in the complex impedance clearly show the contribution of the grain interior and grain boundaries to the electrical response of the material. The equivalent circuit based on the Z-View-software is proposed and the conduction mechanisms are determined. Dielectric data are analyzed using complex electrical modulus M* at various temperatures. The variation of the dielectric parameters (ε’’) is found .Moreover, the temperature dependence study of frequency exponent n (T) is investigated to explain the conduction mechanism in the different range of temperature and frequency.

Keywords: organic salts, crystal structure, Hirshfeld surfaces,^{13}C CP MAS NMR Spectroscopy, optical properties. Electrical conductivity, Conduction mechanism.

1. Introduction

Hybrid materials have been widely explored in recent years as new generation of high performance materials due to their attractive structural, physical and chemical properties **[1-2].** The combination of two different and independently acting compounds into one covalently linked hybrid compound can transfer the synergistic effect of both independently acting moieties to the new composite compound, so that the exclusiveness is greater than the sum of each individual moiety’s proprieties.

This kind of material composed of different components has the advantages of two architectural elements, and therefore produces different structural chemistry [3-6]. This type of material is very large. It is recommended to obtain a variety of different geometric shapes (tetrahedrons, pyramids) through combination, such as sulfate, phosphate, molybdate, nitrate, bromate, perchlorate, etc. [7- 8]. The most studied oxyanion is the Lewis base, which is used as a ligand to prepare interesting metal complexes that have applications in various fields [9-10].

In particular, the combination of nitrate anions and organic molecules (aromatic/aliphatic amino acids) has attracted much attention due to its wide range of applications (biomolecular science, liquid crystals, catalysts) [11-13]. Several organic cations (protonated amines) can be used to stabilize these anions, especially acidic anions **[14-16]**. The organic molecule, such as length, geometry and relative position of the donor groups, play a very important role in interesting three-dimensional networks, layers, chains and ribbon structures **[17-19]**.

Among numerous families of some nitrates, bromated , chlorate salts, we focus on some nitrate, such as $(ClC_7H_6NH_3).NO_3$ **[20]**. , $(ClC_7H_9N)^+(NO_3)^-$ **[20]**. , $(C_8H_{12}NO)\cdot[NO_3]$ **[21]**. and ionic synthesis $[\text{alkyl-Py}]^+[NO_3]^-$ and $[\text{alkyl-MIM}]^+[NO_3]^-$ **[22]**.The atomic arrangement consists of inorganic layers, built from the NO_3^- anions and the organic entities. The major crystal packing was governed by an interconnection with NH…O / C-H…O and C-H…N hydrogen bonds. Due to their ferroelectricity together with dielectric behavior with low band gap [23-24], research on these nitrates has undergone considerable development in recent years.

Intermolecular interactions are present in these hybrid compounds, including electrostatic forces, π-π stacking and hydrogen-bonding interactions. These latter interactions play an important role in the construction of three-dimensional architectures and the stabilization of supramolecular crystal structures and are an important issue that requires focused scientific attention **[20, 25-28].**

Moreover they are rich in hydrogen bonding showing remarkable structural stability, especially at the level of the changes in the dynamics of the cations which are related to the phase transitions. In addition, these compounds are expected to be proton conductors due to the availability of H-bonds. Therefore, they are interesting because of the proton transport mechanisms in biophysical processes and their applications in numerous electrochemical devices, such as batteries, fuel cells, chemical sensors, electrochromic devices, and supercapacitors **[29].**

The cohesion of these materials is generally ensured by hydrogen bonds (N….H … metal/salt) and/or Van Der Waals type of interactions. The long-range order of the ferroelectric type is related to smaller-sized organic cations such as aromatic-entities. Furthermore, the optical properties of these crystals are dependent on the electron configuration of the metal ions, and also on the crystal field associated with the crystal molecular structure.

Impedance spectroscopy appears destined to play an important role in fundamental and applied electrochemistry and materials science in the recent years **[30-33].** In a number of respects, it is the preferred method to characterize the electrical behavior of systems in which the overall system behavior is determined by many strongly coupled processes, each proceeding at a different rate. Furthermore, impedance spectroscopy study provides access to the electrical transport mechanism within the studied compound. The literature has listed an electrical transmission that is ensured by the polaron hopping process. Several theoretical models have been developed to explain the conduction between n blocalized states in the dielectric media who agree on the universal Jonscher's behavior. All these proposed models are based on mechanisms of charge transport by tunneling through a potential barrier or by jump over this barrier **[34-38].** Designing a variety of organic-inorganic hybrid materials perfectly suited to practical applications has been one of the most important challenges. While the transmission of physical properties have been mainly established in organic systems, the ability to exploit the influence of organic molecules such as 1,2-diaminobenzene to structurally modify an hybrid network and consequently induce additional properties remains unexplored in nitrates salts **[20-24]**. The aim of this paper is to study our choice to investigate such materials: we report the synthesis, structural investigations and physical properties of new hybrid salts, $C_6H_4(NH_3)_2(NO_3)_2$.

2. Experimental details

2.1. Chemical preparation:

4.5 ml of 70% HNO_3 (Aldrich) in water was added dropwise to a solution of 1,2-diaminobenzene $C_6H_8N_2$ (67.5 % ; Aldrich; 0.194 g; 2 mmol) a mixture_of an aqueous solution 37% HCl (Aldrich) ; through the reaction in stoichiometric 1:2 .

After stirring for 30 min, it is used to ensure that the compound is completely dissolved. Such solutions were slowly combined in an autoclave and kept at 100°C under auto-genous pressure for 17^h. Good quality of maroon single crystals were obtained suitable for an X-ray structure determination

2.2. Investigation techniques

Characterized by single-crystal X-ray diffraction, powder X-ray diffraction; Hirshfeld surface analysis, IR MAS- NMR spectroscopy and UV–vis spectrophotometry has been reported.

Suitable crystal with size of (0,37*0.12*0.09) mm^3 was selected under an optical examination for structure determination. Intensities and collection data were obtained on a D8 VENTURE Bruker AXS diffractometer equipped with a (CMOS) PHOTON 100 detector using (Mo K_α) radiation (λ= 0.71073 Å) at 150 K. The molecular structure was solved in the monoclinic symmetry ($P2_1/c$, space group) with the lattice parameters: a = 12.6966(17) Å b = 7.9444(11) Å c = 10.3904(14) Å, α = 105.68(0) °,V=1009.05(20) $Å^3$ and Z = 4.

All calculations were made using the WINGX crystallographic suite of programs **[39]**. The crystal structure was determined by the direct method and refined using the SHELXL-SHELXS crystallographic software package **[40, 41].** All non hydrogen atoms were refined with anisotropic atomic displacement parameters. Hydrogen atoms were finally included in their calculated positions and treated as riding on their parent atom with constrained thermal parameters.

The positions of nitrogen, oxygen and carbon atoms have been identified on the subsequent Fourier difference map. A final refinement with 2225 unique intensities and 165 parameters converged to R(F) = 0.0821 et ωR (F^2) = 0.2731 observed reflections with I > 2σ(I).

Crystallographic data are given in **Table 1**. The molecular structure was drawn and presented using ORTEP-3 **[42],** DIAMOND **[43],** Mercury **[44]** and Gauss-view programs **[45].** The fractional atomic coordinates and equivalent isotropic displacement parameters (Å2) are presented in **Table 2; 3**.

The X-ray powder diffraction pattern is recorded at room temperature using a Philips PW 1710 diffractometer operating with copper radiation ($\lambda_{K\alpha 1}$=1.5406A°) in a range of Bragg's angle 5°<2 θ<80°. Unit cell parameters of the synthesized compound were refined by the Rietveld method from powder data.

The intermolecular interactions ensuring the structure cohesion are visualized by Hirshfeld surface **[46]** analysis and the 2D-fingerprint plots, which identify each type of intermolecular interactions.

Molecular Hirshfeld surfaces were constructed from CIF file in order to dissect crystal structures into non-covalent contacts **[47-51]**. Bond lengths to hydrogen atoms were set to standard values. For each point on that iso-surface two distances is defined de, the distance from the point to the nearest nucleus external to the surface, and di, the distance to the nearest nucleus internal to the surface and van der Waals radii (ri^{vdW} and re^{vdW}). Hirshfeld surfaces are mapped using the normalized contact distance (d_{norm}), which is calculated using the following equation **1**:

$$\textbf{eq.:}\ d_{norm} = \frac{d_i - r_i^{vdw}}{r_i^{vdw}} + \frac{d_e - r_e^{vdw}}{r_e^{vdw}} \qquad \textbf{(1)}$$

Thus, the value of d_{norm} was negative or positive when intermolecular contacts were shorter or longer than rvdW, respectively.

NMR-MAS results were performed using a Bruker WB 300 at room temperature. The powdered sample was packed in a 4 mm diameter of rotor and set to rotate at a speed up to 10 kHz in a Doty MAS probehead. During the whole acquisition time, the spinning rate of the rotor was locked in the required value using the Bruker pneumatic unit, which controls both bearing, and driving inlet nitrogen pressures. The ^{13}C spectrum was collected by a cross-polarization of proton with 5 ms contact time. All chemical shifts (δ) are given with respect to tetramethylsilane ^{13}C reference.

FTIR spectra of powder samples were obtained using a 100 Perkin-Elmer FTIR spectrometer from potassium bromide (KBr) pellets. The IR spectrum was recorded in the range of 4000-400 cm^{-1}. UV-vis absorption and optical properties at room temperature are measured by a Perkin Shimadzu, UV-3101PC spectrophotometer using a source emitting wavelength radiation varying between 200 and 800 nm.

The electrical measurements were performed using a two-electrode configuration on a polycristalline sample. The used pellets have an 8mm diameter and 1.2 mm thickness using a hydraulic press at a pressure of 3000 kg/cm^2 used to undertake an electric study. The pellet discs were coated with Ag paste to ensure good electrical contact. After the Ag coating and before measurements the samples were first heated at 100 °C for 12 h under a vacuum. The electrical properties are carried out by means of Solartron1260A Impedance Analyzer coupled with a 1296A Dielectric Interface in the $1–10^6$ Hz frequency range and from 303 to 413K temperature range.

3. Results and discussion

3.1. Crystal structure

The molecular structure properties are discussed on the basis of a single-crystal diffraction investigation. The asymmetric unit of $C_6H_4(NH_3)_2(NO_3)_2$ consists of one discrete diprotonated $(C_6H_4(NH_3)_2)^{2+}$ cation and two crystallographic independent $(NO_3)^-$ anions as shown in **Fig.**

1. We observed the existence of hydrogen bonding in the crystal structure. The molecular geometry and the atom-numbering scheme of this compound are shown in **Fig.1**.

In the molecular arrangement**,** the three H-atoms of two neighboring ammonium group are involved into N-H···O hydrogen bonds. The organic moieties are located between these columns via two kinds of hydrogen bonds **(Fig.3)** relative to C--/N--H/…O**.** The bonding between carbon atoms of (C_6H_4) and oxygen atoms of a mineral (NO_3) is realized by hydrogen bonding C-H…O reported in (Table.5) and shown in (Fig.2).

The title organic-inorganic material is crystallized in the monoclinic system $P2_1/c$ space group Refining the structure in this eccentric space group gives a lattice parameter: a = 12.6966(17) Å b = 7.9444(11) Å c = 10.3904(14) Å β = 105.68(0) ° and V= 1009.05(20) $Å^3$.

Meanwhile, the projection of the molecular arrangement clearly has shown an alternation of $[C_6H_4(NH_3)_2]^{2+}$ cations and $(NO_3)^-$ anions along [001] direction (**Fig. 2**). This alternation is interconnected by hydrogen bonds and π-π interactions from two ($C_6H_4(NH_3)_2$) cation. The organic molecule exhibits a regular spatial configuration with normal C−C and C−N distances and C−C−N and C−N−C angles. Indeed, the C−C bond lengths vary from 1.382(3) to 1.389(2) Å. The mean value of the C−N length is 1.459(3) Å and the C−C−C, C−C−N and C−N−C angles range between 118.44 (17) and 120.89(15)º (**Table.4**). The Bond length and angle values are in good agreement with the bond lengths of the other aromatic salts **[52-54].**

In the studied compound, the ring built up by the atoms from C1 to C6 is planar (the rms deviation of the fitted atoms equals 0.0019(1) Å). The rings of cations stacked between successive anions are approximately parallel to each other and are separated by equal centroid-to-centroid distances **(Fig. 2),** which are too large to be considered as representing π-π* stacking interactions **[55].**

In $(NO_3)^-$ anion, the central nitrogen atom of the mineral anion occupies a special position **(Fig.1)**; an ion is coordinated by three oxygen atoms to form slightly distorted triangle coordination geometry. Selected bond distances and angles are listed in **Table 4**. The N–O distances range from 1.225(3) to 1.302(3) Å. The bond angles show a slight deviation from the ideal value. The angle varies from 117.98(17)-123.95 (17) °. These values are comparable to the corresponding ones previously reported for similar complexes and hybrid salts materials in an organic molecule and mineral anion **[56-59].**

This slight distortion is correlated to deformations resulting from hydrogen bonding interactions (**Table .3**). So, the examination of the structure has shown that the main feature of the atomic arrangement in this compound is the existence of infinite layers composed of anionic and cationic groups parallel to (001) plane at y= n/2, spared by a distance equal to b/2 and linked together by O−H…O and O−H…Cl hydrogen bonds **(Fig.2).** This Figure shows that the anionic entities are interconnected via N−O…H hydrogen bonds to build infinity chains developed along the *c-axis* direction **(Fig. 2).**

Moreover, the organic-entities between these chains via the above-mentioned additional C−H···O hydrogen bonds give rise to this layer (**Table.5**). In the organic entities, the cationic planes arranged on either side of the anions alternately connect the two adjacent inorganic layers cohesion between neighboring layers is assured by means of van der Waals interactions give rise to a three-dimensional network and add stability to the structure. These channels with a pore strong diameter constitute a potential cation-accessible area of the crystal **(Fig. 3).** This organic fits into these channels and interact with means of inorganic framework both electrostatic interactions and via hydrogen bonds.

3.2. X-ray powder diffraction analysis

Fig. 4 shows the powder diffractogram of the C_6 H_4 $(NH_3)_2(NO_3)_2$ hybrid coumpound. The structural refinement of the title compound was analyzed by the Rietveld method via the Fullprof software. For the simulation of the peak shapes, we used the pseudo-Voigt function, and the lattice parameters, which were determined by the Rietveld program and investigated as starting values and by the atomic positional parameters that were derived from Carvajal works **[60].** All the lines observed in this diffractogram are indexed after several optimizations in the monoclinic system (P21/c space group) and the final refining of the compound with lattice parameters: a= 13.086640, b=7.930665 c=10.485829 and β= 106.010°. These values are in good agreement with initial cell parameters obtained by the crystalline structure, which indicate the purity of this synthesis compound.

3.3. Study of intermolecular interactions through Hirshfeld surface analysis

To complete the study of the structural description, we have required the Hirshfeld surface analysis. Recently, a method for studying crystal structures has been developed and involves calculation of molecular surfaces based on Hirshfeld's stockholder partitioning. The Hirshfeld surface plots are generated using the Crystal Explorer software **[62-62]** and represent the partition into molecular fragments of the total crystalline electron density. One of the structural properties that can be mapped onto the Hirshfeld surface is a normalized measure of the distance between atoms, which uses the Van Der Waals radii (rvdW) of the nearest atom inside the surface and the nearest atom outside. The Hirshfeld surface analysis of the title compound was performed using Crystal Explorer 3.1 to figure out the normalized contact distance (d_{norm}), which depends on contact distances to the closest atoms outside (de) and inside (di). For a given crystal structure and set of spherical atomic electron densities, the combination of d_e and d_i in the form of a 2D fingerprint plot provides a summary of intermolecular contacts in the crystal. Complementary regions are also visible in the fingerprint plots where one molecule acts as a donor ($d_e > d_i$) and the other as a recipient ($d_e < d_i$). The contribution of other interactions to the total Hirshfeld surface of the compound has been mapped and exemplified by showing d_{norm} mapping which are depicted in **Fig.5.** 2D fingerprint plots presented in this paper were generated using the reported equation (1) in **[63-64],** which is shown in **Fig 6**. The 2D fingerprint plots can be deconstructed to highlight particular atom pair contacts to separate the contributions from different interactional types that overlap in the full fingerprint **(Fig. 5b) [65].**

The red spots on the around the d_{norm} surface are attributed to the N−O…H, hydrogen bonds, which show the closest intermolecular interactions in the compound. In the shape-index map (**Fig. 6**), the adjacent red and blue triangle-like patches show concave regions that indicate π-π* stacking interactions (H….O/O…H inter-connections) due to the abundance of hydrogen and oxygen on the molecular surface. Overall, H…O contacts are the most favorable (56.4%) in crystal packaging. As previously indicated in **Fig.7**, there are two hydrogen bonds in our crystal structure of the same type N-H...O / C-H...O. However, only the NΦ...$H_{(NO3)}$…$O_{(NO3)}$ contacts appear in this compound, whereas those of H(C(Φ)…O) contacts is low absent, because the atom HΦ is much more electropositive than H($_{(NO3)}$)so is strongly attracted by the electronegative nitrogen atoms. The H…H contacts represented of narrow is symmetric by points with fort de + di Å. Furthermore, they covered 16 % of the total surface of Hirshfeld and represented the second most frequent interactions due to the abundance of hydrogen atoms on the molecular surface.

The HC-CH contacts are the third most frequent interactions (11.8.%) due to the abundance of hydrogen interaction between C_6H_4 molecular on the molecular surface. They constitute the third most occurring contacts, in agreement with the presence of hydrogen bonds of types Φ-H… $O_{(NO3)}$ in this structure.

Finally, the types of contacts O-O / C-C / N-N / CO –CO / NO- NO and NH- NH contribute significantly to the stability of the crystal structure, this value is due to a long interatomic contact and the enriched O…H contacts that are the driving forces in the molecular arrangement and the crystal packing formation. The percentages of contributions for different contacts in the crystal structure of the title material are gathered in **Fig 7**.

In conclusion, visual analysis of intermolecular interactions is consistent with what X-ray diffraction analysis notices. The Hirshfeld surfaces certainly allow a detailed quantitative and qualitative scrutiny by displaying all the intermolecular interactions and specify its placement within the crystal and this methodology has very important promise in crystal engineering. It is obvious that the red regions rich in hydrogen bonds of the d_{norm} surface are in good agreement with the results observed by crystal structure.

3.4. Infrared, NMR -MAS spectroscopy

We have attributed the principal major infrared bands by comparison with similar compounds **[66-70].** The infrared spectrum was performed at room temperature as shown in **Fig.8.** The bands located at 3235 and 3280 cm^{-1} in IR are ascribed to symmetric and asymmetric stretching of NH. Those observed at 3150 and 2345 $cm^{-1}$are assigned to the symmetric and asymmetric stretching of CH. The band observed around 1600 $cm^{-1}$is attributed to the stretching of C=C. Those observed at 1031 and 1070 cm^{-1} associated with the vibration of β (CH) and stretching of CN, respectively. However, the bands observed around 537-620 cm^{-1}regioncorrespond of the β (C-C-C) and β (C-C), respectively. In addition, the region average 650 to 730 cm^{-1} are characterized by the sharp doublet which due to the ώ(NH2) and γ (CH), γ(CC) , respectively. Finally, the bands observed at 1180 and 1292 cm^{-1}correspond to =C-H vibrations.

The isotropic band of the ^{13}C cross-polarization magic angle spinning nuclear magnetic resonance (CP-MAS-NMR) spectrum of a crystalline $C_6H_4(NH_3)_2(NO_3)_2$ sample rotating at the magic angle with a frequency of 10 kHz is given in **Fig.9**. According to the IUPAC convention, shielding corresponds to negative values.

The simulation of the isotropic band permits the identification of three peaks, observed in 126.7, 127.2 and 129.5 ppm, using Gaussian and lorentzian functions by means of a dmfit program **[71]**. This resonance region are corresponding to three equivalent aromatic carbons of the organic-groups. This result proves the presence of only one entity in the asymmetric unit cell of the compound, a result in good agreement with crystallographic data.

On the other hand, the peaks at around 129.5 ppm can attributed to the C-atoms connected to the ammonium groups of $(NH_3)^+$. Finally, the two peaks at 126.7 and 127.2 ppm relative to the two groups CH external in aromatic carbons. It is worthwhile noting that the chemical shift values are as commonly observed as in aniline derivatives **[72-76].**

3.5. Gap energy

To evaluate the gap energy of the synthesized compound, the optical measurement was investigated. **Fig. 10** shows the experimental UV–vis absorption spectrum of

$C_6H_4(NH_3)_2(NO_3)_2$ at room temperature. As seen, there are four distinct absorption peaks at 213, 278,332 and 350 nm, which are very comparable to those found in other materials previously reported to contain organic– inorganic hybrid compound, such as **[77-78].**

The obtained spectra show a sharp increase in absorption at wavelengths near the absorption edge of the threshold wavelength for the onset of absorption at 213 nm.

In hybrid compounds based on aromatic ring, the π-π^* transition of benzenoid ring is observed around 278 nm, this result is agreement with similar compounds (λ = average 300 nm) was observed in the literature **[79-80]**.

Additionally, the observed absorptions at 332 and 350 nm are caused by band gap absorption and they are attributed to the excitation of free electron–hole pairs within the mineral anion and higher energetic level in the conduction band. This suggests that the compound behaves as semiconductor material and is compatible with the orange color of the crystal (orange).

The optical absorption edge is a significant parameter for describing solid-state materials. Also, for disordered materials is interpreted in terms of direct or indirect transition through an optical band gap. For absorption by direct or indirect transition, the absorption coefficient (α)which is defined as the decrement ratio of incident radiation relative to unit length in the direction of wave propagation in the medium is related to the absorbance (A) through the follow equation **2**: $\boldsymbol{\alpha = \frac{2.303A}{d}}$; **(2)**; where d is the sample thickness and A the absorbance.

The optical band gap (Eg) is related to absorption coefficient (α) and photon energy (hv) through the Tauc relation **(Eq.3) [81]:** $\mathbf{(\alpha h\upsilon)=B(h\upsilon-Eg)^n}$ **(3)**

where B is constant, hυ is the photon energy, Eg is optical band gap and n is the index, which takes different values depending on the mechanism of inter band transitions n= 2 and ½ corresponding to indirect and direct transitions, respectively. The energy hυof incident photon, which can be calculated using the equation **4 [82-83]**: $\mathbf{h\upsilon = 1240 / \lambda(nm)}$ **(4)**

In addition, there is an index determined by the nature of the electronic transitions during the absorption process. The transition is called direct when the extremity of V.B and C.B is located at the same k-space ($\Delta k=0$), while the transition is called indirect when the transition possible only with phonon assisted ($\Delta k\neq0$) **[84]**.

Fig. 11 shows the plots of $(\alpha h\nu)^2$ as a function of photon energy (hν) for $C_6H_4(NH_3)_2(NO_3)_2$ compound. The shapes of these curves favor the direct transition. Therefore, the hybrid salt compound has a direct band gap. The optical energy gap Eg can be determined by the extrapolation of the curve until the energy axis. The calculated values of Eg equal to 5.03 eV.

The Urbach energy Eu is a very important parameter to characterize the disorder of a material. It corresponds to transitions between extended states of the valence band and localized states of the conduction band. Bougrine et al. **[85]** interpreted the Urbach energy Eu, as the width of the bands localized states in the band gap. From the variation of the absorption coefficient, it is possible to deduce the disorder in the compound. Thus, the absorption coefficient is associated with the disorder by the empirical relationship **(Eq.5) [86]**:

$$\boldsymbol{\alpha = \alpha_0\, exp\left(\frac{h\upsilon}{E_u}\right)} \textbf{(5)}$$

By plotting Lnα as a function of energy hυ, we can access the value of E_u. Where α is a constant a E_u is the Urbach energy. The value of E_u is calculated from the inverse of the slope of versus **[87]**, seen in **Fig. 12**. The dependence of the optical absorption coefficient with photon energy may arise from electronic transitions between localized states.

3.6. Electrical impedance analysis

3.6.1. Equivalent circuit, Nyquist plots

The impedance spectroscopy technique play a major part and is suitable to investigate electrical conductivity and to analyze the charge transport processes in grains and grain boundaries in materials in terms of thermal and frequency ranges. This is accomplished by modeling the sample through an equivalent circuit that produces an electrical simulation of the sample’s electrical properties and relaxation **[88].** Moreover, the presence of nonstoichiometric oxygen greatly changes the electrical properties of the material. It is also known that the size of granules decreases as a result of reduction and their number increases. It follows that the intergranular contribution should predominate in reduced samples **[89-91].** Z′ and Z″ are the real and imaginary parts of complex impedance. The relations with parameters of real and imaginary offer a wide scope for a graphical analysis of the various parameters under different experimental conditions (temperature, frequency,etc.) **[92–94].** The impedance spectra obtained at different temperatures are shown in **Fig. 13** in the temperature range 373-413 K and the frequency range 209 HZ to 5 MHZ. In the studied temperature range, Z’–Z’’ arcs move to a lower value of impedance when the temperature increases. The bulk ohmic resistance values of the sample can be determined from the intercept of the semicircle, at low frequency, with the real axe (Z’) .There are mainly two overlapping semicircles observed in each impedance spectrum. The low frequency semicircle is due to the grain boundary and the higher one depicts the grain **[95].** To understand the electrical properties and to determine the equivalent circuit of this compound we recorded the Nyquist diagrams as well as the frequency variation of Z' and Z" at different temperatures in the **Fig. 14**. The observed dispersion instead of a centered semicircle on the real axis indicates a non-Debye type of relaxation **[96]**. These spectra show broad one semicircle indicate the overlap of the grain and grain boundaries response. The simulate Nyquist diagrams based in the Z-view logical show the equivalent circuit reported in the **Fig. 14** described well the behavior of this material. This circuit is modeled by a combination parallel of the resistance R which described the response of the grain and grain boundaries, capacity C and fractal capacity CPE. There is a good agreement between simulated and experimental data, which confirms that the proposed equivalent circuit describes the electrical properties of the sample. The extracted values of the resistance R are used to determinate the conductivity of the grain and grain boundary. Therefore, the parameters obtained by the simulation enable us to represent the variation of conductivity $(\boldsymbol{\sigma_g = e/SR_g})$ as a function of temperature described by the law of Arrhenius **(Eq.6)**: $\boldsymbol{\sigma_g = \sigma_0\ e\text{-}(E_a/K_BT)}$ **(6)**; where **Ea** is the activation energy, σ is the conductivity. It is obtained from Z_0 by means of the relation **7**: $\boldsymbol{\sigma = e/Z_0S}$ **(7)**, where **e/S** represents the geometrical ratio sample, *A* is the pre-exponential factor, *k*b is the Boltzmann constant and **T** is the temperature. The dependence of conductivity as function temperature recorded in the **Fig. 15**. Shows a change in the slope curve with activation energy equal to 0.37 $(\mathbf{d_i})$ and 2.3 $(\mathbf{d_{ii}})$ eV respectively. Consequently, the conduction is explained by the thermally activated mechanism. The equivalent circuit selection is confirmed by **Fig. 16-17** showing the variations of the experimental values of (Z') and (-Z") as a function of the simulated data, using the parameters obtained from the equivalent circuit model. The slope obtained from linear fit for these curves at each temperature is very close to unity. Good compatibility between experimental and theoretical data indicates that the equivalent circuit used reasonably describes the electrical properties of the studied compound. The variation of both (Z') and (-Z") with the frequency**,** at different temperatures, is presented respectively in the inset of **Fig. 16-17**. We may notice that the values of (Z') and (-Z") increase (T 〈373 K) and decrease (T〉 373 K) with the increase of temperature for.

3.6.2. Electric Modulus formalism

The complex modulus formalism has been used in the analysis of the electrical properties in particularly suitable to extract phenomena such as electrode polarization and conductivity relaxation times. The complex electric modulus can be represented by the following equation **(Eq.8-9) [97-100]:**

$$M^* = 1/\varepsilon^* = M' + iM'' \quad \textbf{(8)}$$

$$M^* = M_\infty \left[1 - \int_0^\infty e^{-jwt} \left(-\frac{d\varphi(t)}{dt} \right) dt \right] \quad \textbf{(9)}$$

Best fits for M'' at different temperatures is shown in **Fig. 18.** M" reaches a constant value M∞ (M∞ =1/ε∞) at high frequencies for all temperatures and this is due to the relaxation processes, which are spread over a range of frequencies. This plot shows that at low angular frequencies the values of M'' approaching zero indicating that the electrode effect can be neglected in the modulus representation **[101].** The peaks in the M" plots shift toward higher frequencies and their height increase with increasing temperature. The asymmetric M'' plot is suggestive of stretched exponential character of relaxation times of the material. It is observed that the peak frequencies M''_{max} shift toward the high frequency side with an increase in temperatures, indicates a thermally activated dielectric relaxation process in which the hopping mechanism of charge carriers dominates intrinsically. This peak indicates the transition from long-range to short-range movement with an increase in frequency. The observed width of the peaks indicates the non-Debye behavior of the material **[102].**

3.6. 3. Frequency and temperature dependence of AC conductivity

The AC conductivity gives detailed information about the time-dependent movements of charge, which leads to conductivity and investigate the dielectric relaxation/dispersion phenomena. The frequency variation of the ac conductivity, $\sigma_{ac}(\omega)$, at various temperatures is shown in **Fig. 19**. Electrical conduction is thermally an activated process according to Josher's Universal Dispersion Relaxation (UDR) and the origin of the frequency dependence of the conductivity is related to the relaxation due to the mobile charge carriers **[103].** The electrical conductivity follows the power law **(Eq.10)**:$\boldsymbol{\sigma_{ac}(\omega) = \sigma_{dc} + A(\omega)^n}$ **(10)**

where, σdc represents dc. conductivity, A is a pre-exponential constant and n is the power law exponent, where $0 < n < 1$ which presents the degree of interaction between mobile ions and the environment surrounding them **[104]**. In fact, σ_{ac} increases with the increase of frequency, which is a characteristic of ω^n. The variation of n, as a function of temperature, reflects the changes in the conduction mechanism at a temperature range shown in **Fig. 20**. The observed behavior of n with (1-n) is in agreement with the conduction model where the exponent decreases with increasing temperature up to a minimum and then increases **[105- 106].** In the course of studies, it was found that the grain size has a measurable effect on most dielectric properties. For example, at room temperature, hardness, yield strength, tensile strength, fatigue strength and impact strength all increase with decreasing grain size. Mass transport, and especially oxygen vacancies transport, destroys the grains **[107-108].**

3.6.3. Frequency dependence of the dielectric permittivity

The measured impedance is used to calculate the imaginary (ε’’) parts of the complex dielectric permittivity as **[109] (Eq.11-12)**:

$$\varepsilon'(\omega) = \varepsilon_\infty + \frac{(\varepsilon_s - \varepsilon_\infty)[1 + (\frac{\omega}{\omega_1})^{1-\alpha}\cos(\frac{(1-\alpha)\pi}{2})]}{1 + 2(\frac{\omega}{\omega_1})^{1-\alpha}\cos(\frac{(1-\alpha)\pi}{2}) + (\frac{\omega}{\omega_1})^{2(1-\alpha)}} \qquad \textbf{(11)}$$

$$\varepsilon''(\omega) = \frac{(\varepsilon_{s-\varepsilon_\infty})(\omega/\omega_1)^{1-\alpha} sin\left(((1-\alpha)\pi)/_2\right)}{1+2(\omega/\omega_1)^{1-\alpha} cos\left(((1-\alpha)\pi)/_2\right) + (\omega/\omega_1)^{2(1-\alpha)}} + \frac{\sigma_0}{\varepsilon_{0\omega}} \qquad \textbf{(12)}$$

Fig.21. shows the frequency dependence of the dielectric constant ε’’(ω) at fixed temperatures. As the temperature increases, the dielectric constants at low frequency show a dispersive behavior since in the low frequency region of the ε’’spectrum a clear tail connected to the conductivity was observed. Best fits using the function (6) give a suitable fitting of the curves resulting from the experimental data.

In the present case, the conduction losses predominate at lower frequencies, and hence, at all temperatures, the imaginary part of the permittivity ε” shows 1/ω dependence on angular frequency. ε” is also found to increase with increasing temperature, and the dielectric loss peak has not been observed. The common method of getting dielectric loss peak in solid electrolytes is through separating dc conductivity from the total conductivity σ(ω). However, in ionically conducting materials, at low frequencies, there is an inevitable electrode polarization effects, and the dielectric constant is rather high. This often gives rise to lots of experimental errors during the separation of dc conductivity from the total conductivity. However, the data were converted into electric modulus where the contributions from the electrode effects are minimized **[110–112]. Fig. 22** shows the tangent losses, tan

$\delta=\varepsilon''(\omega)/\varepsilon'(\omega)$, as a function of frequencies at different temperatures. All the curves show a similar behavior at frequencies above 100 kHz. Nevertheless, at frequencies below 100 kHz, an intense increase of dielectric loss was observed for all measurement temperatures. This type and frequency dependence of Z' and Z" and suggest the presence of dielectric relaxation in the compound **[113-114].**

4. Conclusion

In conclusion, we have successfully synthesized a new organic-inorganic compound $C_6H_4(NH_3)_2(NO_3)_2$. Structural parameters and data refinement have been analysed by single crystal X-ray diffraction. The crystal structure can be described by alternation built by nitrate anions $(NO_3)^-$ and diprotonated $C_6H_4(NH_3)_2)^{2+}$ cations . The crystalline packing of the compound is stabilized by hydrogen bonding interactions N-H...O / C-H...O. The geometric intermolecular characteristics were quantified by the Hirshfeld surface analysis. The ^{13}C MAS NMR spectrum is in agreement with the X-ray structure and all observed IR bands were examined in this investigation. Optical absorption shows a direct band gap of 5.03 eV.

The AC conductivity and electric behavior of compound have been studied as a function of temperature and frequency. The frequency dependent conductivity of materials at different temperatures has been analyzed using a Jonscher's power law expression and the temperature independent frequency exponent term has been evaluated. The analysis of the temperature variation of M’’ peak indicates that the observed relaxation process is thermally activated.

References

[1] Zhao, X. H., Huang, X. C., Zhang, S. L., Shao, D., Wei, H. Y., & Wang, X. Y. Journal of the American Chemical Society, 43(2013) 16006-16009..
[2] Zhang, Y., Ye, H. Y., Zhang, W., & Xiong, R. G. Inorganic Chemistry 1 (2014) 118-123.
[3] Lukianova, T. J., Kinzhybalo, V., & Pietraszko, A. Acta Crystallographica Section E: Crystallographic Communications, 11 (2015). 191-192.
[4] Bednarchuk, T. J., Kinzhybalo, V., Bednarchuk, O., & Pietraszko, A. Journal of Molecular Structure, 1120 (2016)138-149.
[5] T. J. Bednarchuk, V. Kinzhybalo, A. Pietraszko, Acta Cryst. C72 (2016) 432–441
[6] Z. Czapla, S. Dacko, A. Waskowska, (2003) J. Phys. Condens. Matter. 15(2003)3793–3803.
[7] L S Eder D J watkin A Cousson J Applied cryst 37 (2004)545-550.
[8] I Bayar L Khedhiri S Soudani J. Mol. Struct 1161(2018) 185-193.
[9] Mohga F. Mostafa, Shimaa S. Elkhiyami, Seham A. Alal, Materials Chemistry and Physics, 202 (2017) 159–168.
[10] Rawhi Al-Far, Basem F. Ali,and Khaldoun Al-Sou’oud, Journal Chemical Crystallography, 8(2006) 36-38
[11] L. S. Èder, D. J. Watkin, A. Cousson, Richard Ian Cooper and Werner Paulusc, J. Appl. Cryst. 37(2004)545-550.

[12] P. Czarnecki, W. Nawrocik, Z. Pajaxk & J. Nawrocik, J. Phys. Condens. Matter. 6, (1994) 4955–4960.

[13] I. Bayar, L. Khedhiri, S. Soudani, F. Lefebvre, P.S. Pereira da Silva, C. Ben Nasr, J. Mol. Struct. 1161(2018) 185-193.

[14] A. Rayes, C. Ben Nasr, M. Rzaigui, Mater. Res. Bull. 39 (2004) 1113-1121.

[15] K. Kaabi, C. Ben Nasr, M. Rzaigui, J. Phys. Chem. Solids 65 (2004) 1759-1764.

[16] H. Rahmouni, W. Smirani, M. Rzaigui, S.S. Al-Deyab, Acta Cryst E66 (2010) o993.

[17] K. Kaabi, M. El Glaoui, V. Ferretti, M. Zeller, C. Ben Nasr, Acta Cryst E67 (2011) 2507-2508

[18] L. Bendjeddou, A. Cherouana, N. Hadjadj, S. Dahaouib, C. Lecomteb, Acta Cryst E65 (2009) o2303- o2304.

[19] C. Peng, Acta Cryst E66 (2010) o2214

[20] R. Hakiri, I. Ameur, S. Abid, N. Derbel, J. Mol. Struct. 1164 (2018) 468-492

[21] I. Bayar, L. Khedhiri, S. Soudani, F. Lefebvre, P.S. Pereira da Silva, C. Ben Nasr, Journal of Molecular Structure, 18(2018)30178

[22] J.E.Castellanos-Águila,M.A.Olea-Amezcua,H.Hernández-Cocoletzi,M.Trejo-Durán , Journal of Molecular Liquids 285 (2019) 803-810.

[23] S. Soudani, V. Ferretti, C. Jelsch, F. Lefebvre, C. Ben Nasr, J. Solid State Chem. 237 (2016)7–13

[24] Imen Bayar, Lamia Khedhiri, Ramzi Fezai, Pedro Sidonio ,Pereira da Silva, Manuela Ramos Silva, Cherif Ben Nasr , J. Mol. Struct. 1181(2019) 300-304

[25] T. Sahbani, A. Chiheb Dhieb, W. Sta Smirani, M. Rzaigui, Phase Transitions. 141(2016)1594-1597.

[26] S. Gatfaoui, A. Mezni, T. Roisnel, H. Marouani, J. Mol. Struct. 93 (2017) 23-28.

[27] S. Soudani, V. Ferretti, C. Jelsch, F. Lefebvre, C. Ben Nasr, J. Solid State Chem. 237 (2016) 7–13

[28] K. Klai, K. Kaabi, W. Kaminsky, C. Jelsch, F. Lefebvre, C. Ben Nasr, J. Mol. Struct. 1128(2017) 378-384.

[29] V.B. Kapustianik, S.A. Sveleba, R. Tchukvinskyi, Y. u. Korchak, V. Mokryi, I.I. Polovinko, Z. Trybula, Phys. Stat. Sol. 151 (1995) 481–488.

[30] R. Ben Said, B. Louati, K. Guidara, , Ionics 20 (2014) 209–219.

[31] S.R. Elliott, N.F. Mott,J. Adv. Phys. 18(1969) 41.

[32] S. Sen, R.N.P. Chaudhary, Mater.Chem. Phys. 87 (2004) 256.

[33] J. Suchanicz, Mater. Sci. Eng. B .55(1998) 114.

[34] B. Louati, K. Guidara, Mater. Sci. Eng. B 177 (2012) 838– 843.

[35] H. Mahamoud, B. Louati, F. Hlel, K. Guidara, J. Alloys Compd. 509 (2011) 6083–6089.

[36] R. Ben Said, B. Louati, K. Guidara, Ionics 20 (2014)703–711.

[37] C. BenMohamed, K. Karoui, S. Saidi , K. Guidara, A. BenRhaiem, Physica B 451(2014) 87–95.

[38] A. Kahouli, A. Sylvestre, F. Jomni, B. Yangui, J. Legrand, J. Phys. Chem. A 116 (2012) 1051–1058.

[39] L.J. Farrugia, WinGX suite for small-molecule single-crystal crystallography, J. Appl. Cryst. 32 (1999) 837-838.

[40] G.M. Sheldrick, SHELXS-97, Program for Crystal Structure Solution and Refinement, University of Gottingen, Germany, 1997.

[41] G.M. Sheldrick, SHELXL-97, Program for Crystal Structure Solution and Refinement, University of Gottingen, Germany, 1997.

[42] C.K. Johnson, ORTEP: a FORTRAN Thermal-Ellipsoid Plot Program for Crystal Structure Illustrations, Report ORNL-3794, 1965.

[43] K. Brandenburg, Diamond. Visual Crystal Structure Information System. Version 3.2i, Crystal Impact GbR, Bonn, Germany, 2012.
[44] C.F. Macrae, P.R. Edgington, P. McCabe, E. Pidcock, G.P. Shields, R. Taylor, M. Towler, J. Van de Streek, J. Appl. Cryst. 39 (2006) 453-457.
[45] A. Frisch, R. Dennington II, T. Keith, J. Milliam, A. Nielsen, A. Holder, J. Hiscocks, Gauss-view Reference, Version 4.0, Gaussian Inc., Pittsburgh, 2007.
[46] M.A. Spackman, J.J. McKinnon, CrystEngComm 4 (2002) 378-392
[47] S.K. Seth, D. Sarkar, T. Kar, CrystEngComm 13 (2011) 4528.
[48] S.K. Seth, D. Sarkar, A.D. Jana, T. Kar, Cryst. Growth Des. 11 (2011) 4837.
[49] A.A. Prasad, K. Muthu, V. Meenatchi, M. Rajasekar, R. Agilandeshwari, K. Meena, J.V. Manonmoni, S.P. Meenakshisundaram, Spectrochim. Acta A 140 (2015) 311.
[50] Z. Yousefi, H. Eshtiagh-Hosseini, A. Salimi, A. Janiak, J. Mol. Struct. 1038 (2015) 460-470.
[51] P. Manna, S.K. Seth, M. Mitra, A. Das, N.J. Singh, S.R. Choudhury, T. Kar, S. Mukhopadhyay, CrystEngComm 15 (2013) 7879-7886.
[52] M. Belhouchet, W. Wamani, T. Mhiri, Journal of IOP Conference Series: Materials Science and Engineering, 13(1) (2010)012039.
[53] A.Jellibi, I. Chaabane, K.Guidara, Journal of Polyhedron, 89(2015) 11-18
[54] I.Mkaouar,N.Karâa, B. Hamdi, R. Zouari, Journal of Molecular Structure 1115(2016)161- 170.
[55] B. Kulicka, R. Jakubas, Z. Ciunik, Solid State Sci. 8 (10) (2006) 1229- 1236.
[56] Imen Bayar, Lamia Khedhiri, Frederic Lefebvre, Valeria Ferretti, Cherif Ben Nasr, Journal of Molecular Structure, 18(2018)31281
[57] I. Bayar, L. Khedhiri, S. Soudani, F. Lefebvre, P.S. Pereira da Silva, C. Ben Nasr, Journal of Molecular Structure, 18(2018)30178
[58] I. Bayar, L. Khedhiri, S. Soudani, F. Lefebvre, V. Ferretti, C. Ben Nasr, Journal of Molecular Structure 18(2018) 30184
[59] Cong Zhang, Ya Feng, Chen Shen, Guoping Yong, Chemical Physics Letters, 659 (2016) 176–181.
[60] J.R. Carvajal, Recent advances in magnetic structure determination by neutron powder diffraction, Physica B. 192 (1993) 55–69.
[61] F. L. Hirshfeld, Bonded-atom fragments for describing molecular charge densities,Theoretica. Chimica. Acta. 44 (1977) 129-138.
[62] S.K. Wolff, D.J. Grimwood, J.J. McKinnon, M.J. Turner, D. Jayatilaka, M.A. Spackman, CrystalExplorer. University +9of Western Australia, Perth, 2012.
[63] M.A. Spackman, J.J. McKinnon, J.Cryst Eng Comm ,4 (2002) 378-392.
[64] J. Janczak, G.J. Perpetuo, J.Acta Cryst. C57 (2001) 123–125.
[65].M.D.Ye M L Hu C.P Ye Z Kristalloger.2017 (2002) 501-502.
[66] F. Zouari , A.Ben Salah, Journal of Solid State Sciences, 6(2004)847- 851
[67] R. Elwej, N. Hannachi, I. Chaabane, A. Oueslati, F. Hlel, Journal of Inorganica Chimica Acta, 406 (2013) 10-19.
[68] R. Elwej, A. Bulou, F. Hlel, Journal of Synthetic Metals, 222(2016),372- 382.
[69] M.Hamdi,A.Oueslati,I.Chaabane,F.Hlel,Journal of ISRN Condensed Matter Physics, , 750497(2012)1-8
[70] N.Sundaraganesan,C.Meganathan,M.Kurt,Journal of Molecular Structure, 891(2008)284- 291.
[71] D. Massiot, H. Theile, A. Germany, Bruker Rep 43 (1994) 140.
[72] H.C. Galka, L.H. Gade, Inorg. Chim. Acta 357 (2004) 1725.
[73] W. Wamani, R. Elwej, T. Mhiri, M. Belhouchet, Journal of Advances in Chemistry, 5(2013)741-752.

[74] R.Hajji ,A. Oueslati, ,N. Errien, F. Hlel, Journal of Polyhedron, 79(2014)97-103.
[75] H.C. Galka, L.H. Gade,Journal of Inorganica Chimica Acta,357(2004) 1725- 1732.
[76] R. Elwej, N. Hannachi, K. Adil, F. Hlel, Journal of Phosphorus, Sulfur, and Silicon and the Related Elements, 187(2012) 1173- 1182.
[77] W. Wang, X. Chen, S. Efrima, J. Phys. Chem. B 103 (1999) 7238.
[78] A. Kessentini, M. Belhouchet, J.J. Suñol, Y. Abid, T. Mhiri, J. Mol. Struct. 1039 (2013) 207.
[79] G. R. Kumar. J. Vivekanandan. A. Mahudeswaran. P. S. Vijayanand. Iran Polym J 22 (2013) 923-929.
[80] A. Abkari, I. Chaabane, K. Guidara, Physica E: Low-dimensional Systems and Nanostructures 86(2017) 210-217
[81] S.K. Gagandeep, B.S. Lark, H.S. Sahota, Nucl. Sci. Eng. 134 (2000) 208.
[82] D.N.Neman, "Semiconductors physics and devices basic principles" R.D.Irwin, Inc. (1992).
[83] Moh and E Davic, "Electronic process in non-crystalline material" 2nd ed. Universe, press Oxford (1979).
[84]. W. Cei, and D. Srivastava, Appl. Phys. Lett., 85,12 (2004) 2208.
[85] A. Bougrine, A. El Hichou, M. Addou, J. Ebothé, A. Kachouna, M. Troyon, Material Chemistry and Physics 80 (2003) 438.
[86] G.D. Cody, Semiconductors and Semimetals, edited by J. I. Pankove Academic, 1984, 21B, Chap. 2.
[87] F. Yakuphanoglu, A. Cukurovalib, I. Yilmaz, Opt. Mater. 27 (2005) 1363.
[88] H. Sondes, C. Iskandar, G. Kamel, , RSC Adv. 6 (2016) 91649–91657,
[89] S.V. Trukhanov, I.O. Troyanchuk, N.V. Pushkarev, H. Szymczak, , JETP 95 (2002) 308-315.
[90] M.V. Zdorovets, A.L. Kozlovskiy, Vacuum 168 (2019) 108838
[91] Orilukas A, Dindune A, Kanepe Z, Ronis J, Kazakevicius E, Kezionis A (2003). Solid State Ionics 157:177.
[92] Macdonald JR (ed) 1987 Impedance spectroscopy, Wiley.
[93] Kremer F, Schönhals A (2002) Broadband dielectric spectroscopy. Springer, Berlin.
[94] Vassilikou-Dova A, Kalogeras IM 2009 Dielectric analysis (DEA), in thermal analysis of polymers, fundamentals and applications, (eds: Menzel JD, Prime RB), Differential scanning calorimetry (DSC). chapter 6, pp 497–614 Wiley, Hoboken.
[95] T. Badapanda, R.K. Harichandan, S.S. Nayak, A. Mishra, S. Anwar, J. Proc. Appl. Ceram. 3(2014) 145-153.
[96] S. Sen, R.N.P. Choudhary, P. Pramanik, Physica B 387 (2007) 56–62.
[97] P.B. Macedo, C.T .Mognihan, R .Bose, Phys Chem Glasses .13 (1972) 171.
[98] M. Ganguli, M. Harish Bhat, K. Rao, J Phys Chem Glasses .40(1999) 297
[99] S.Lanfredi, P.S.Saia, R .Lebullenger, A.C. Hernandes, Solid State Ionics .146 (2002) 329-339.
[100] S. Ghosh, A. Ghosh , Solid State Ionics. 149 (2002) 67-72.
[101] P. Thongbai, B. Putasaeng, T. Yamwong, V. Amornkitbamrung, S. Maensiri, J. Alloys Compd 582 (2014) 747-753.
[102] B. Louati, K. Guidara, M. Gargouri, J. Alloys Compd 472 (2009) 347-351.
[103] G.C. Psarras, E. Manolakaki, G.M. Tsangaris, Compos. Part A 34 (2003) 1187–1198.
[104] M. Ben Bechir, K. Karoui, M. Tabellout, K. Guidara, A. Ben Rhaiem. Journal of Alloys and Compounds 588 (2014) 551–557.
[105] J.T. Gudmundsson, H.G. Svavarsson, S. Gudjonsson, H.P. Gislason, Phys. B 340 (2003) 324-328.
[106] M. Krimi, K. Karoui, A. Ben Rhaiem. Journal of Alloys and Compounds 698 (2017)

510-517.
[107] S.V. Trukhanov, L.S. Lobanovski, M.V. Bushinsky, V.V. Fedotova, I.O. Troyanchuk, A.V. Trukhanov, V.A. Ryzhov, H. Szymczak, R. Szymczak, M. Baran, J. Phys.: Condens. Matter 17 (2005) 6495-6506.
[108]. M.V. Zdorovets, A. Arbuz, A.L. Kozlovskiy, Ceram. Int. 46 (2020) 6217-6221
[19] Suchanicz J Mater Sci Eng B 55(1998) 114-417.
[110] Chen SA, Liao CS Macromolecules 26(1993) 2810-2816.
[111] Tsangaris GM, Psarras GC, Kouloumbi N ,J Mater Sci 33(1998) 2027-2037.
[112] Nowick AS, Lim BS ,J NonCryst Solids 172(1994) 1389-1400.
[113] Williams G, Watts DC ,Trans Faraday Soc 66(1970) 80
[114] Bauerle JE ,J Phys Chem Solids 30(1969) 2657.

Credit Author Statement

Manuscript title: The $C_6H_4(NH_3)_2(NO_3)_2$ assembly **investigations : Crystal structure , Optical properties and** impedance spectroscopy, electrical relaxation with Ac conductivity studies.

These are the standard contribution roles:

- **Conceptualization:** N. HANNACHI
- **Data curation :** N. HANNACHI
- **Formal analysis:** N. HANNACHI, F. HLEL
- **Funding acquisition:** N. HANNACHI, F. HLEL
- **Investigation:** N. HANNACHI, T. ROISNEL
- **Methodology:** N. HANNACHI, F. HLEL
- **Project administration:** N. HANNACHI
- **Resources:** N. HANNACHI

- **Software:** N. HANNACHI, F. HLEL
- **Supervision :** N. HANNACHI, F. HLEL
- **Validation:** N. HANNACHI, T. ROISNEL
- **Visualization :** N. HANNACHI
- **Roles/Writing – original draft :** N. HANNACHI
- **Writing – review & editing:** N. HANNACHI, F. HLEL, T. ROISNEL
- The submission of the manuscript has been approved by all co-authors.

Yours Faithfully,

Prof. N. HANNACHI

DCOI

Hello I am pleased to send you this article for examination

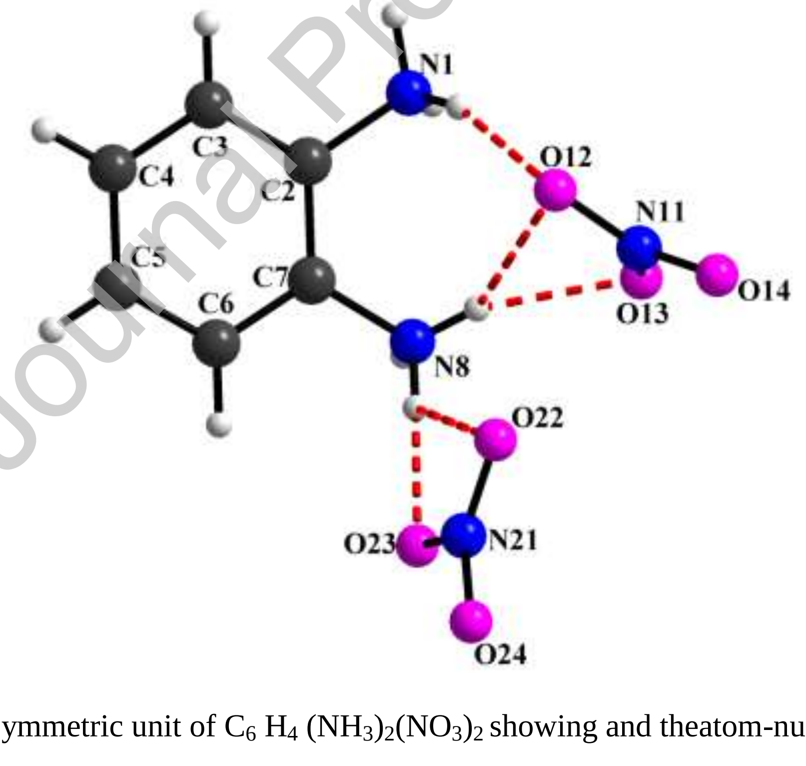

Figure.1 : Asymmetric unit of C_6 H_4 $(NH_3)_2(NO_3)_2$ showing and theatom-numbering scheme

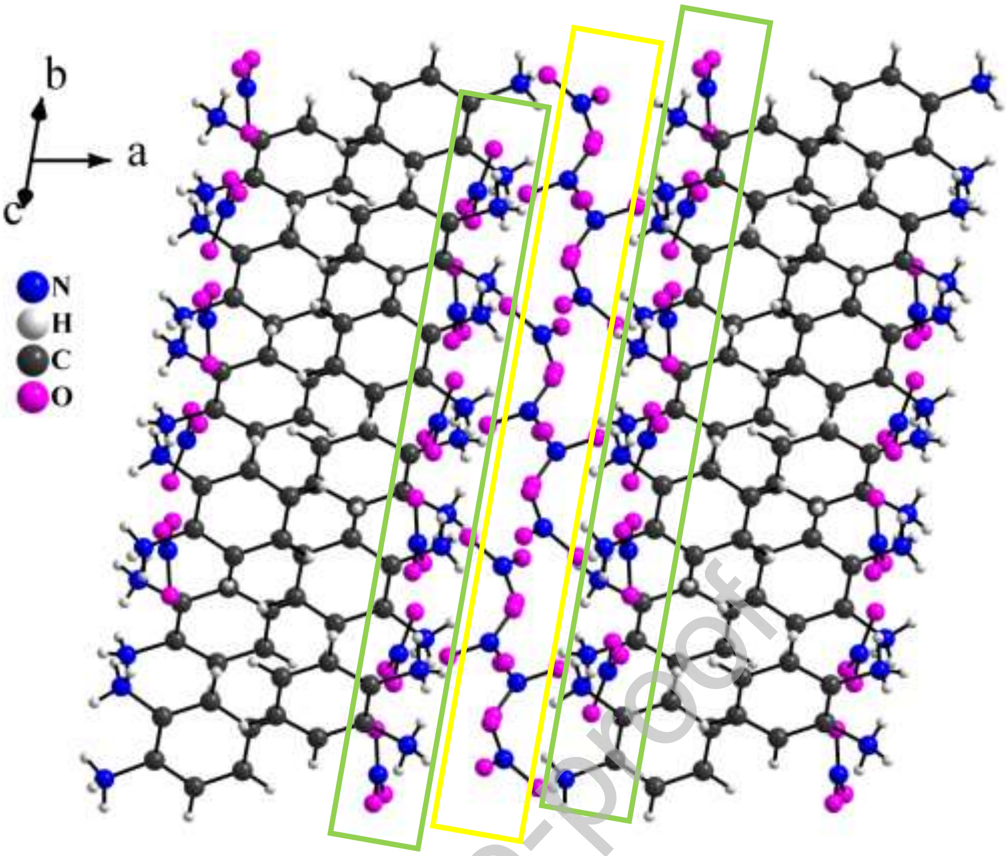

Figure2: Overall view of the crystal paking a long (001) plan.

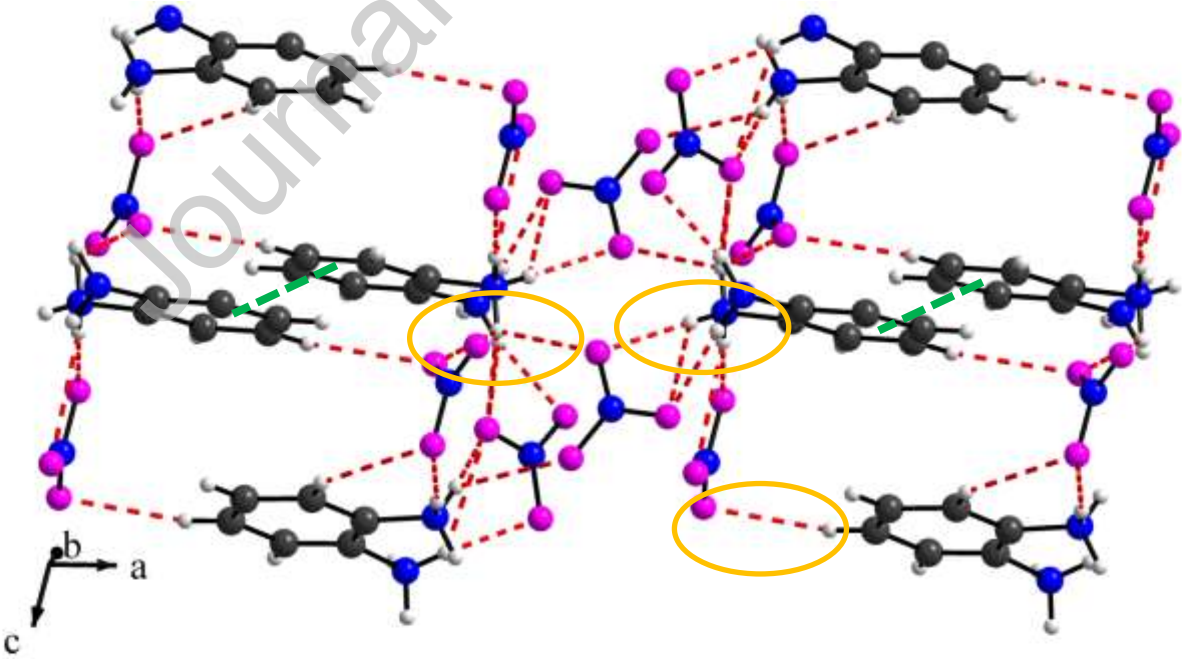

Figure.3: the paking diagram of C_6 H_4 $(NH_3)_2(NO_3)_2$ along c-axis the dashed lines stand fort the hydrogen-bonds (red) with π-π*interactions.

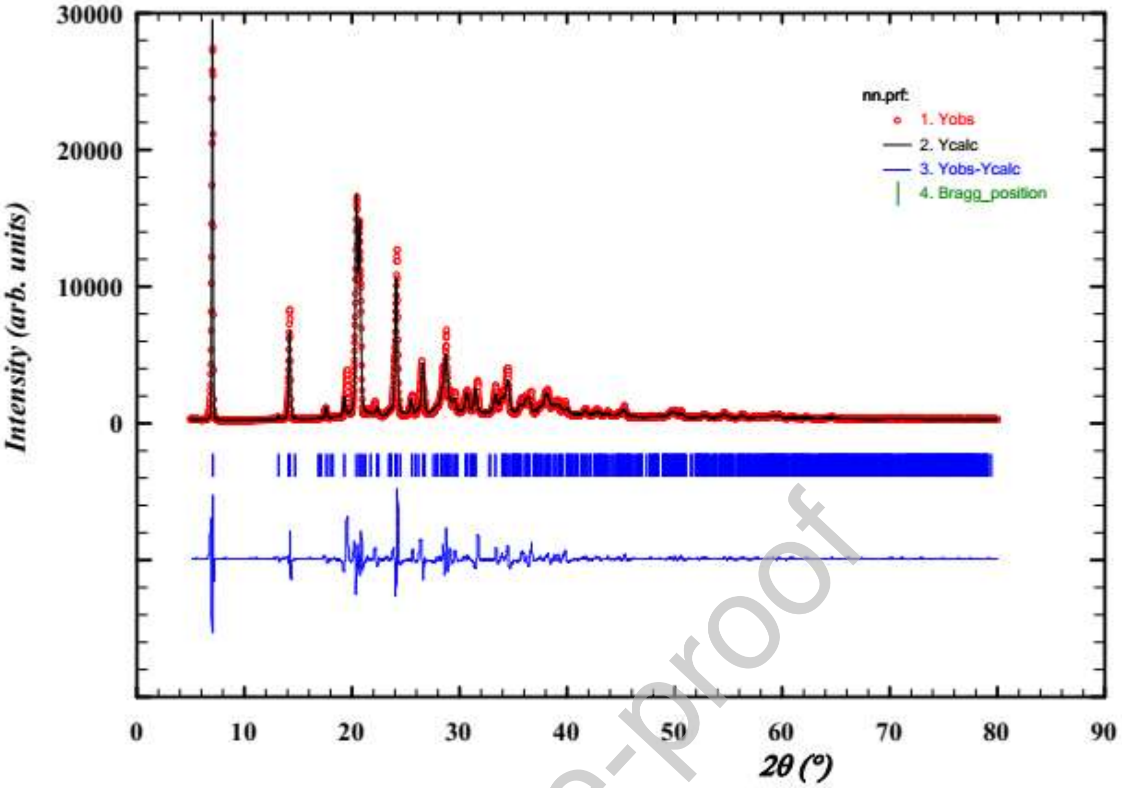

Figure.4: Refinement X-ray powder diffractogramm of $C_6 H_4 (NH_3)_2(NO_3)_2$ by Rietfeld method.

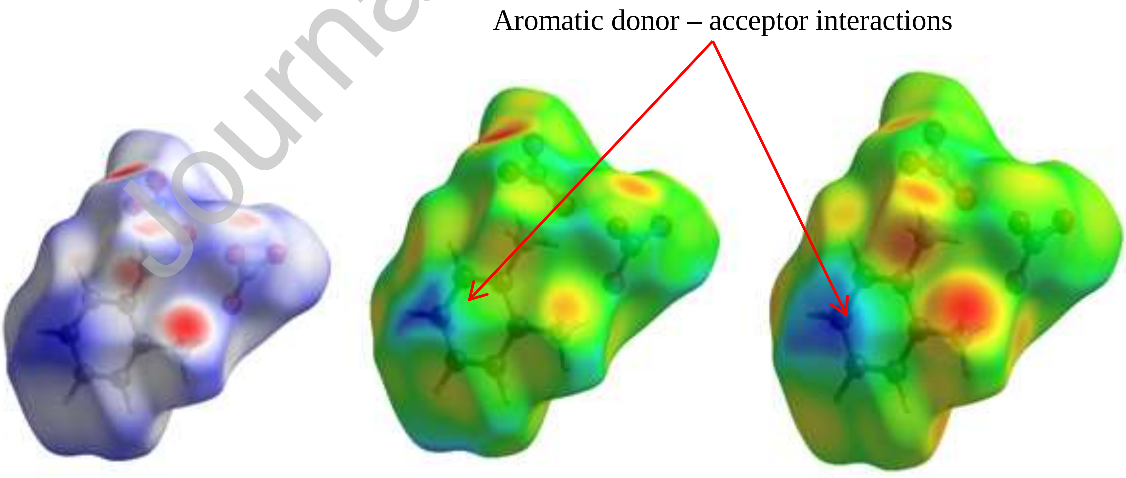

(a) **(b)** **(c)**

Figure 5: Hirshfeld surface of $C_6 H_4 (NH_3)_2(NO_3)_2$: (a) dnorm, (b) de and (c) di.

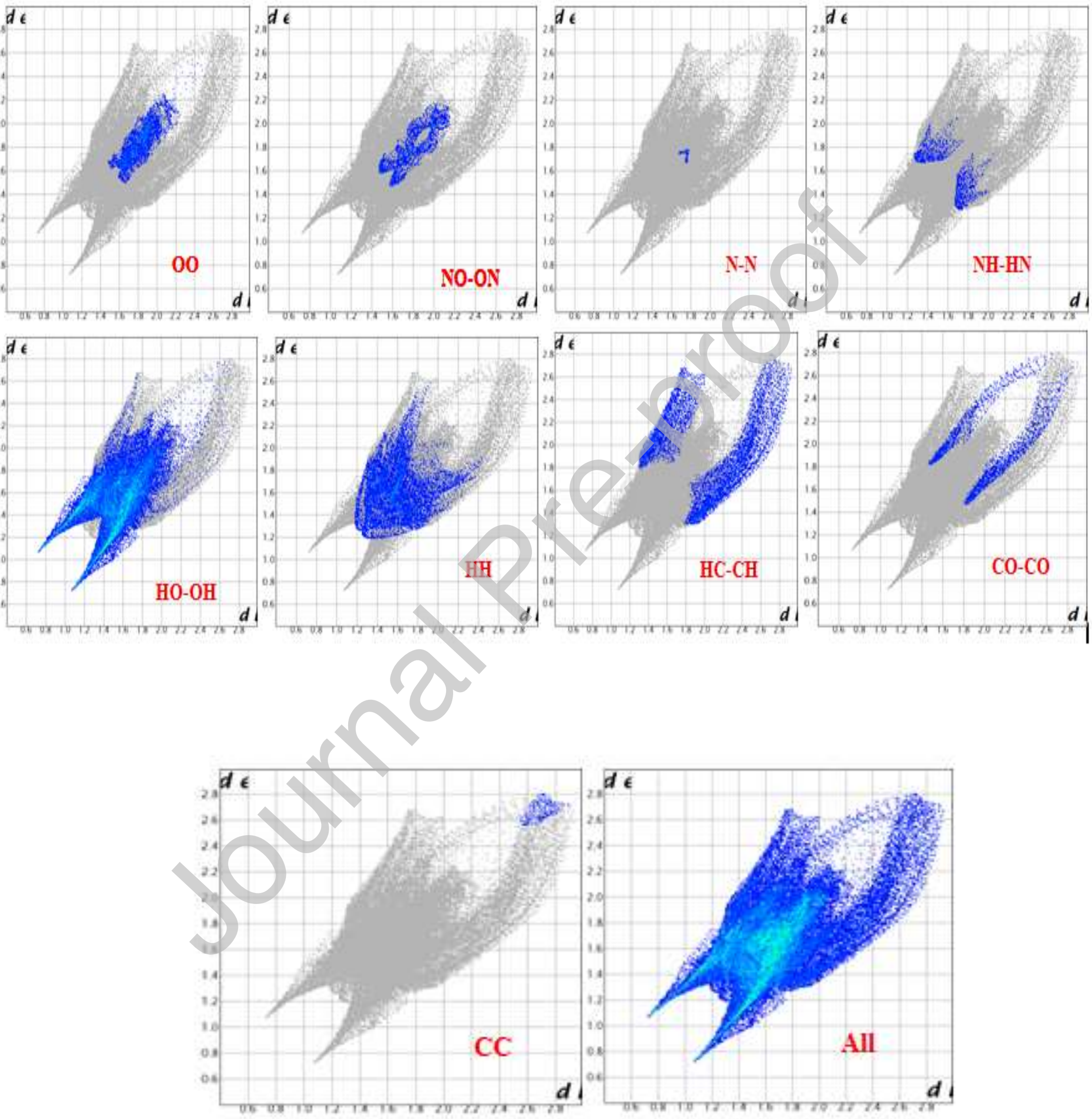

Figure 6 : Finger-print plots of C_6 H_4 $(NH_3)_2(NO_3)_2$.

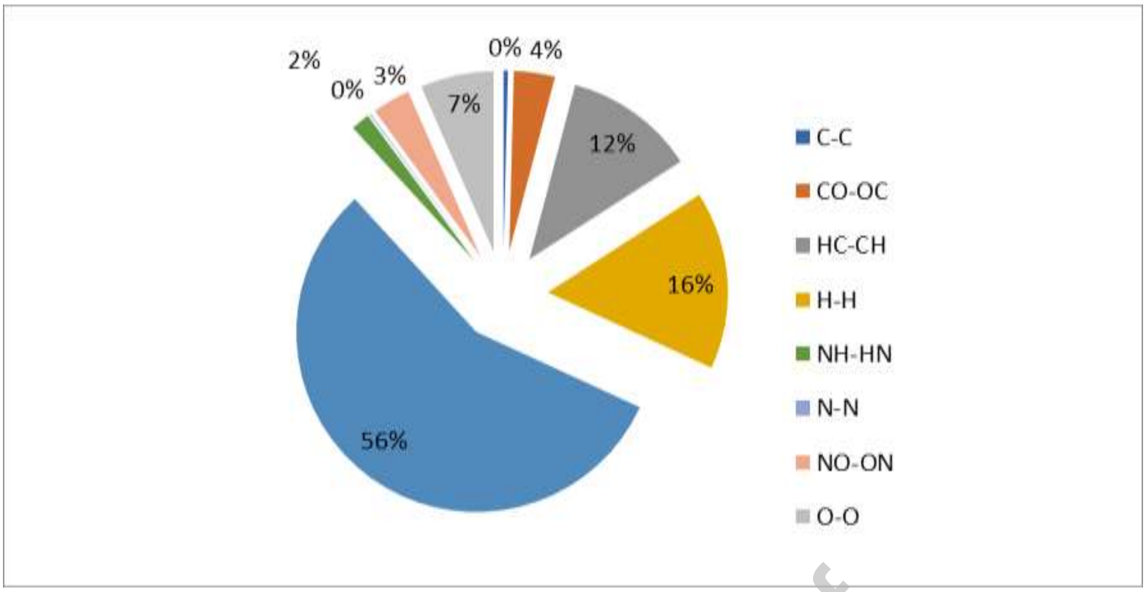

Figure 7 : Decomposed finger-pint plots of major contacts.

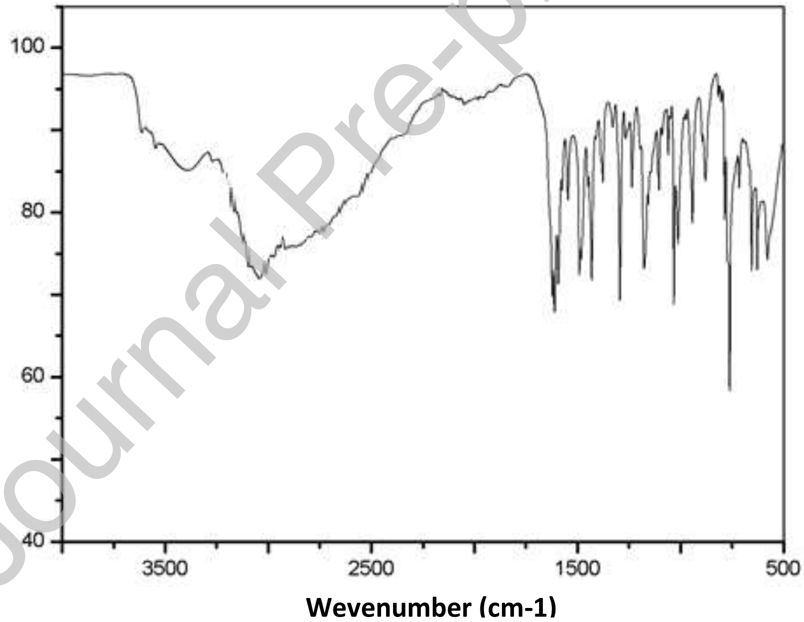

Figure 8: Experimental FTIR spectra of $C_6 H_4 (NH_3)_2(NO_3)_2$ at room temperature.

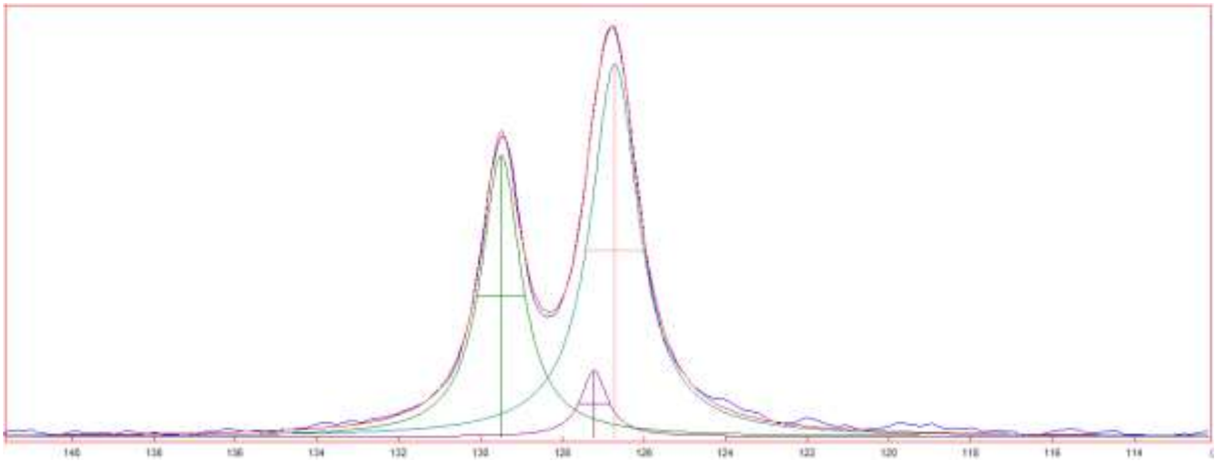

Figure 9: Plots of experimental and fitted curves of the isotropic band of the ^{13}C CP-MAS.

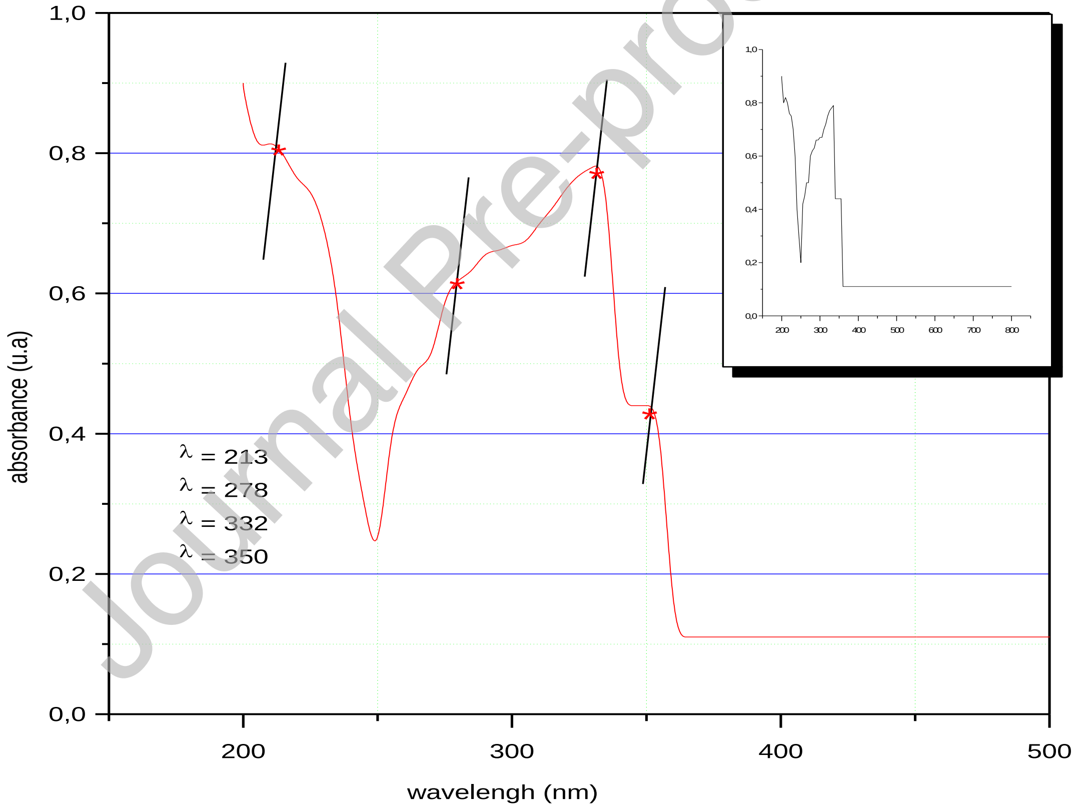

Figure 10. Absorbance spectra for $C_6 H_4 (NH_3)_2(NO_3)_2$

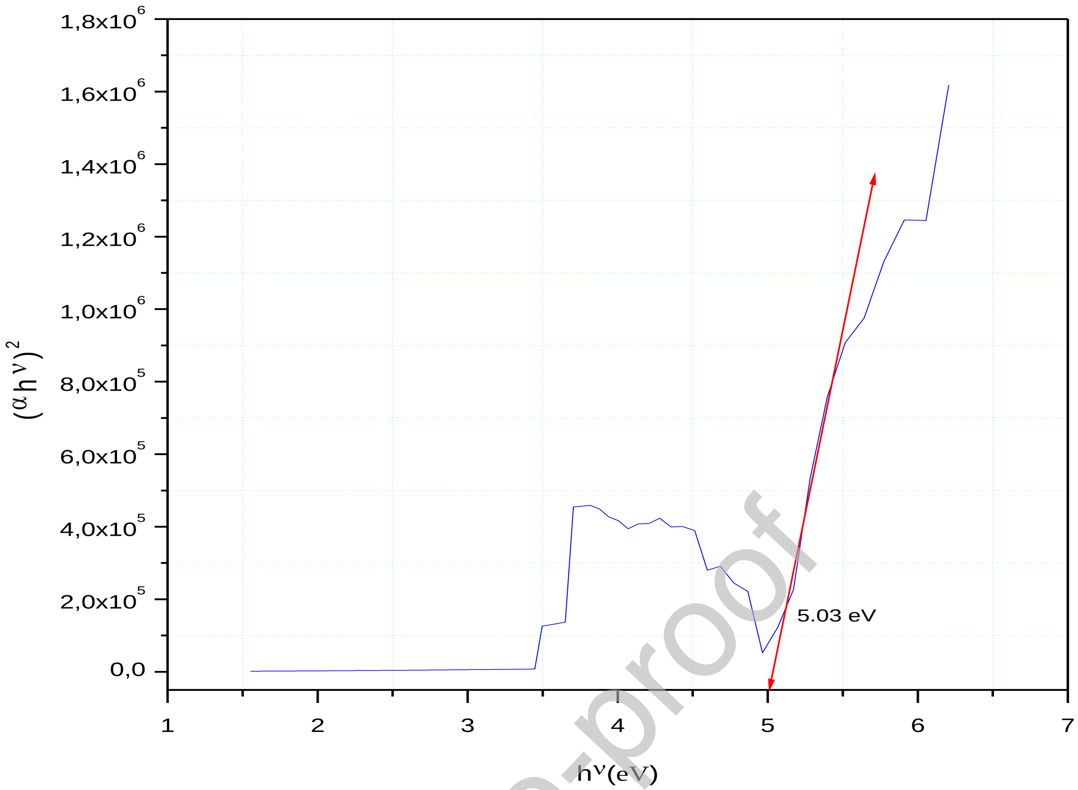

Figure 11. Taucs plots of $C_6\ H_4\ (NH_3)_2(NO_3)_2$.

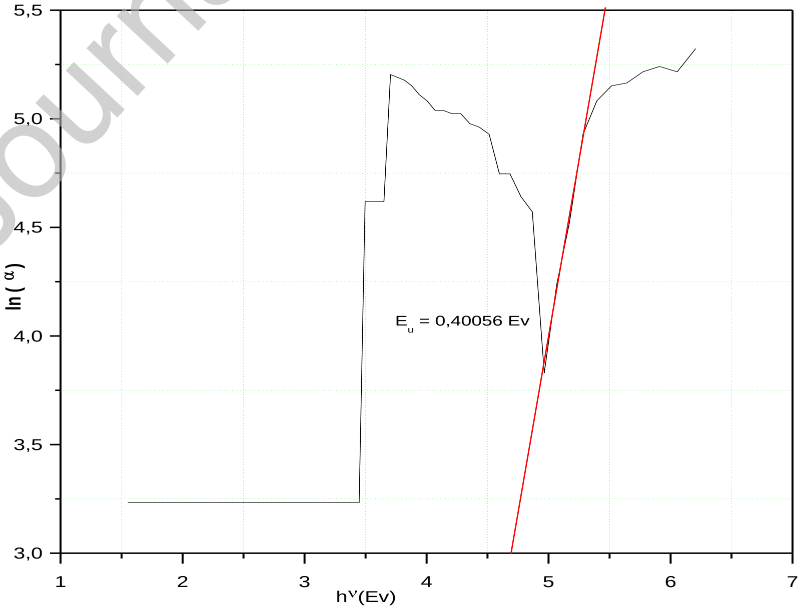

Figure 12. Determination of Urbach energy for $C_6\ H_4\ (NH_3)_2(NO_3)_2$

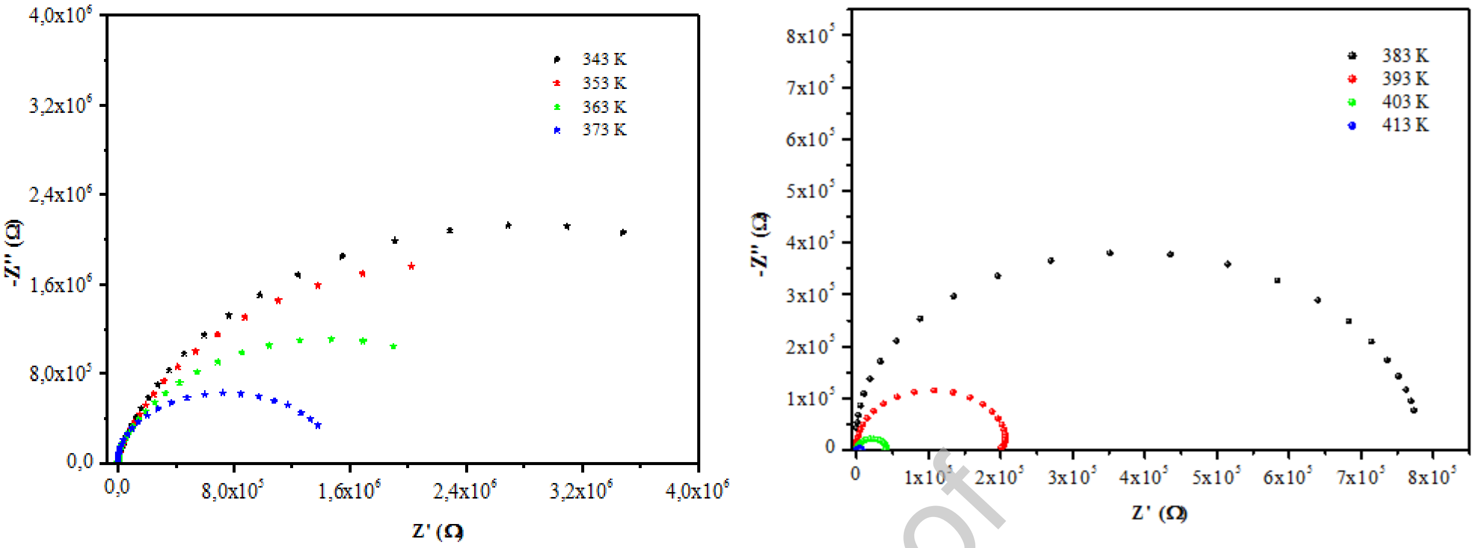

Figure 13: Plots of impedance complex at various temperatures

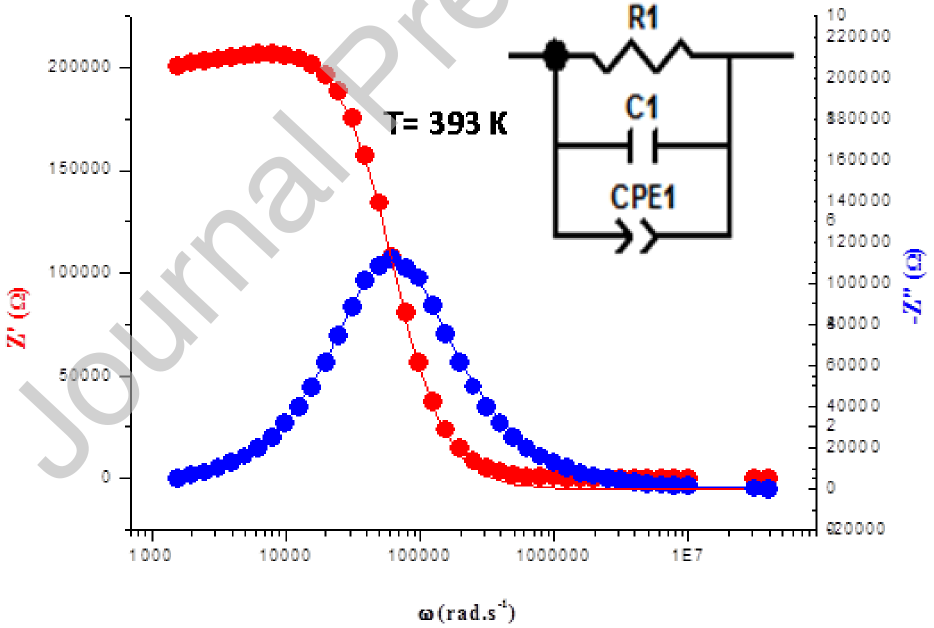

Figure14: Simulated Nyquist plots with equivalent circuit of the $C_6H_4(NH_3)_2(NO_3)_2$ coumpound at different temperatures.

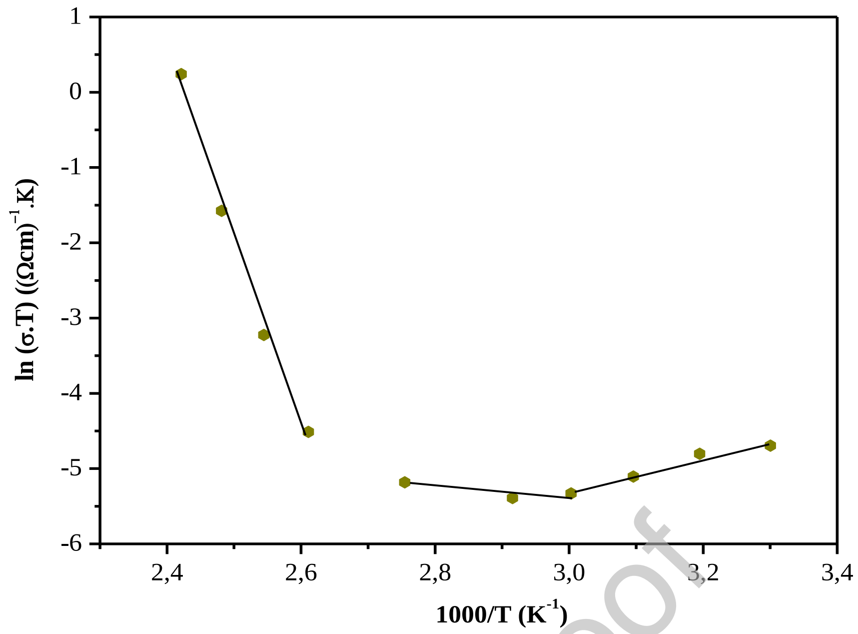

Figure 15: variation of σ as function of temperatures of $C_6H_4(NH_3)_2(NO_3)_2$

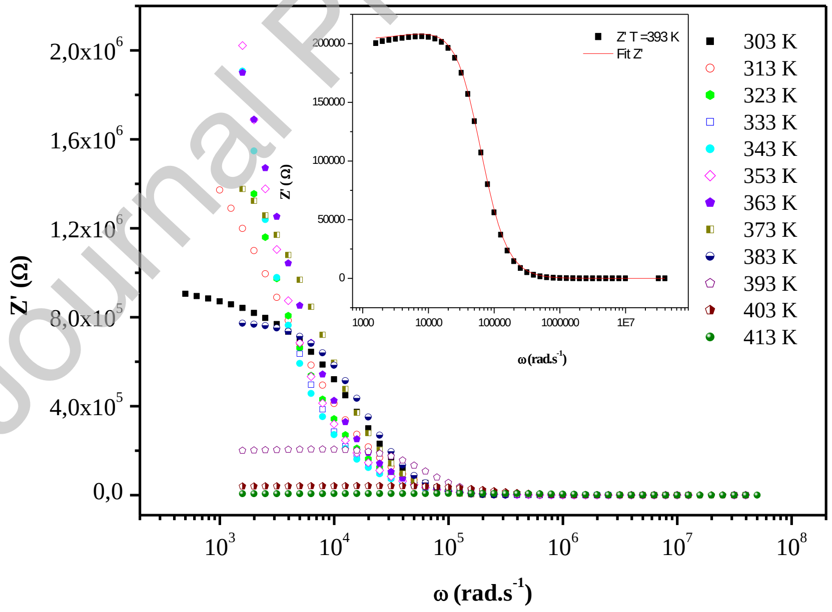

Figure 16: Variation of real part of the impedance as a function of frequency for some representative temperature

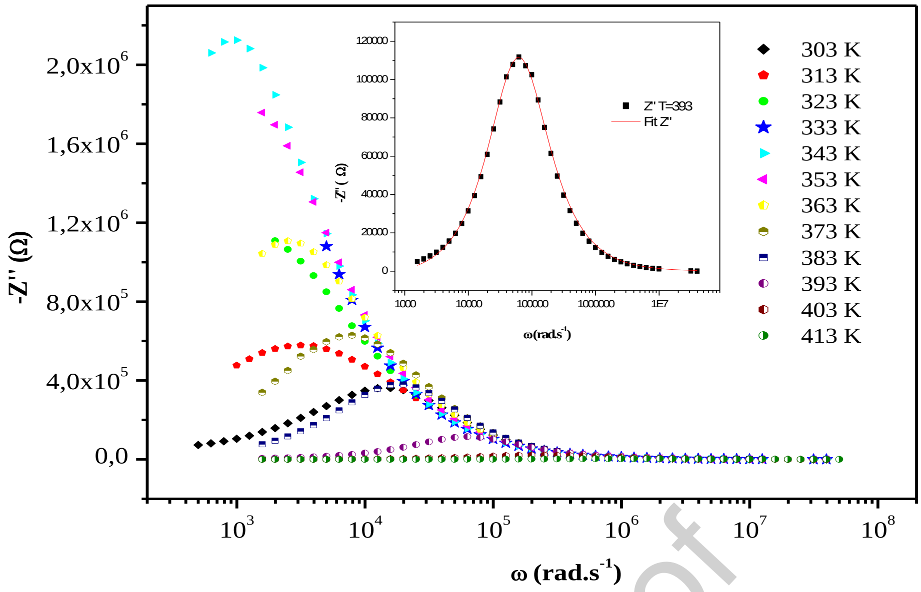

Figure 17: Variation of imaginary part of the impedance as a function of frequency for some representative temperature

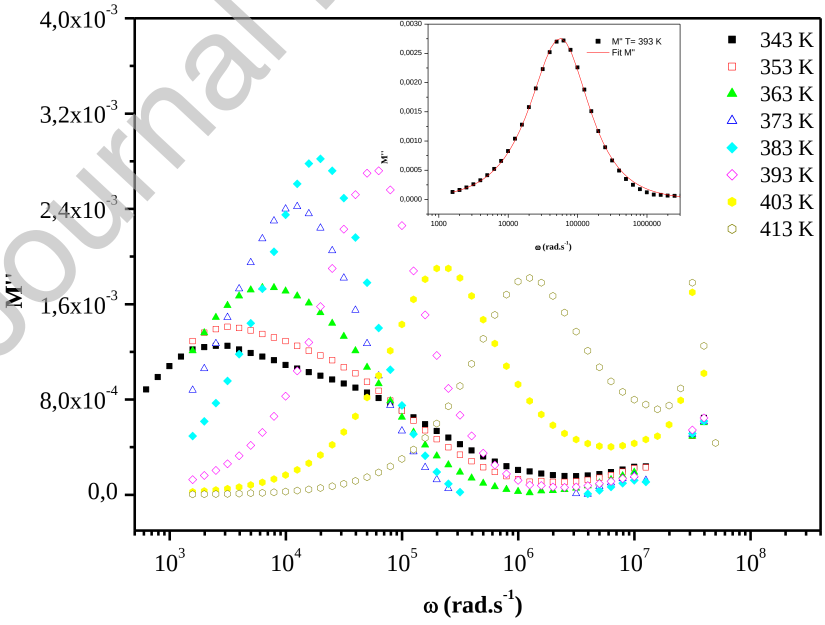

Figure 18: Variation of M″ as a function of the frequency at various temperatures with best fit.

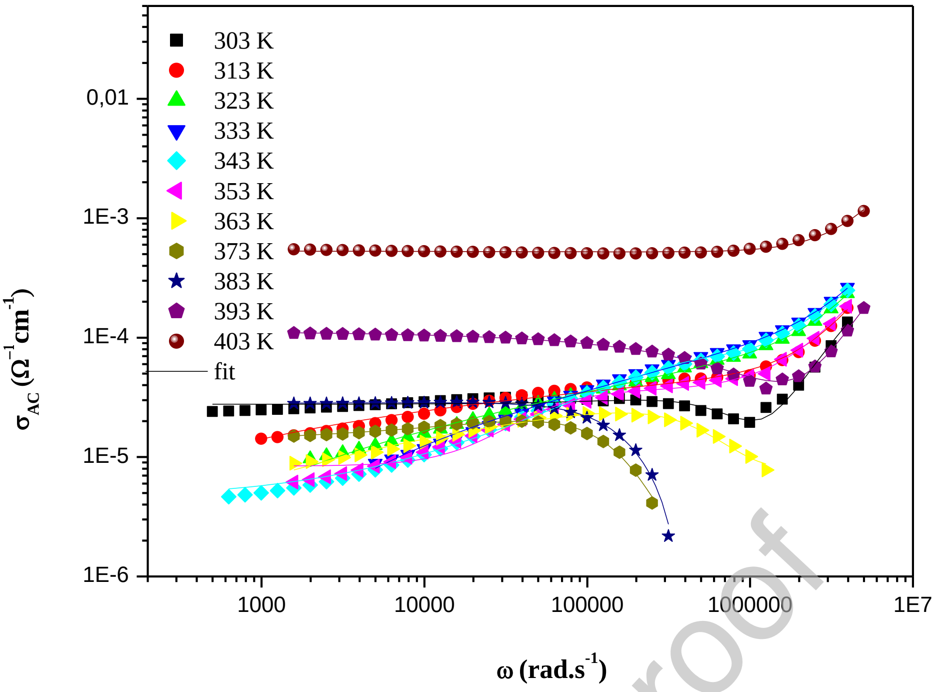

Figure 19 : Frequency dependencies of the ac complex conductivity at several temperatures

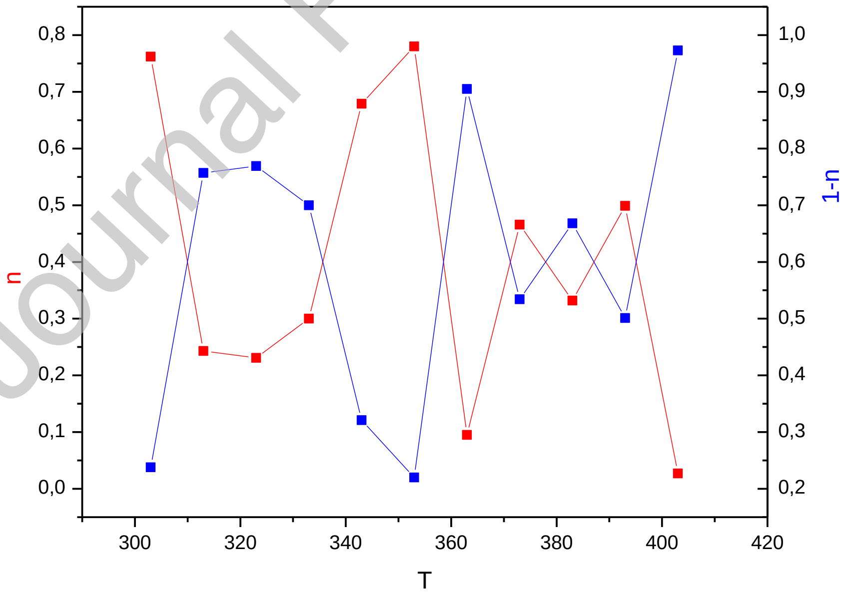

Figure 20 : Correlations between n and 1-n at several temperatures

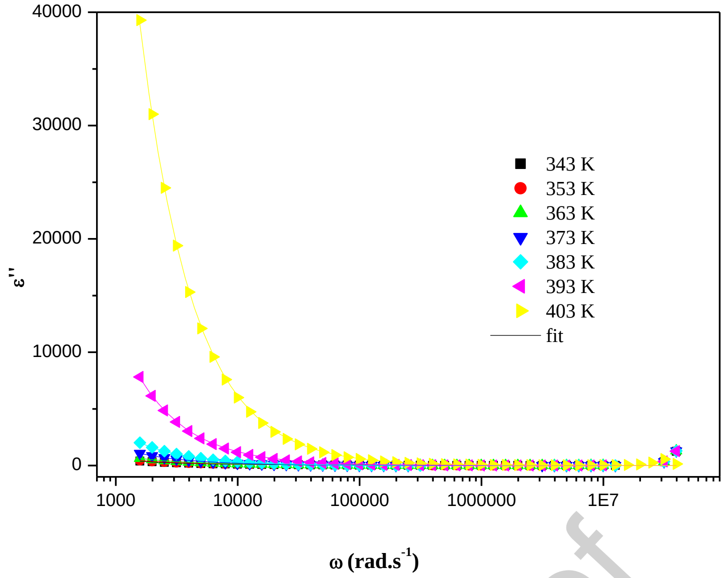

Figure 21 : Frequency dependence of the dielectric loss ε''(ω) at various temperatures

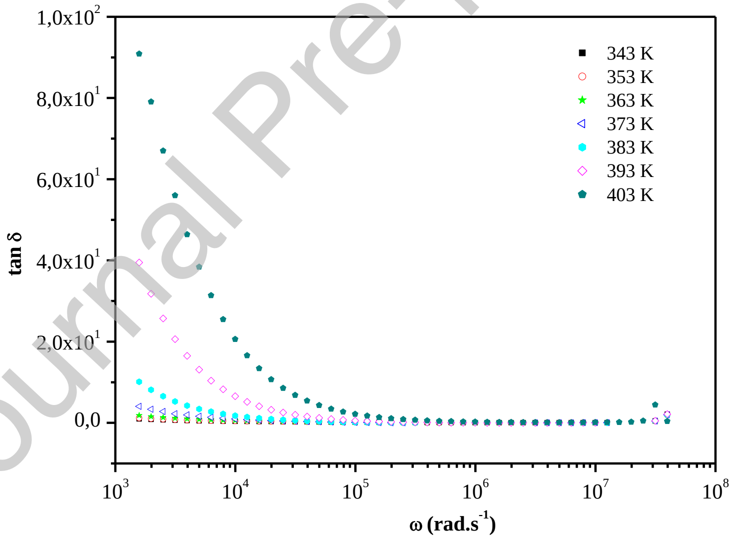

Figure. 22 : Variation of the tangent losses (tan δ) versus frequency at several temperatures

Table 1: Summary of crystal data and structure refinement

Complex Empirical formula	$C_6 H_4 (NH_3)_2(NO_3)_2$
Formula weight (g.mol^{-1})	*243.18*
Crystal system/ Space group	*Monoclinic, P 1 21/c 1 (no. 14)*
Temperature (K)	*150*
Unit cell dimensions	
a (Å)	*2.6966(17)*
b (Å)	*7.9444(11)*
c (Å)	*10.3904(14)*
β (°)	*105.68(0)*
V (Å^3)/ Z	*1009.05(20)/ 4*
Radiation	*Mo Kα*
μ (mm^{-1})	*0.703*
h, k, l ranges	$-7 \le h \le 9$ $-18 \le k \le 18$ $-10 \le l \le 10$
Crystal size (mm)	*0.37 × 0.12 × 0.09*
Reflections collected / unique / observed reflections [$I > 2\sigma(I)$]	*3745 / 976 / 930*
R_{int}	*0.0345*
$(\sin \theta/\lambda)_{max}$ (Å^{-1})	*0.649*
Structure refinementwith	*SHELXL-97*
Goodness of fit	*1.333*
Final R and Rw	*0.033/0.108*
Refinement	F^2 *full matrix*
Refinedparameters	*56*
$\Delta\rho_{max}$, $\Delta\rho_{min}$ (e Å^{-3})	*0.988 /0895*
	w=1/[\s^2^(Fo^2^)+(0.0544P)^2^+0.3015P] *where P=(Fo^2^+2Fc^2^)/3*

Table 2: Atomic coordinates and isotropic displacement parameters (in Å ^{2})

Atom	**x**	**y**	**z**	**U**
N1	0.32274(13)	0.0696(2)	0.42714(18)	
H1A	0.3474(19)	0.100(3)	0.356(2)	0.0170
H1B	0.370(2)	0.083(3)	0.498(3)	0.0170
H1C	0.3129(18)	-0.042(3)	0.413(2)	0.0170
C2	0.22092(15)	0.1596(2)	0.41903(18)	
C3	0.12459(16)	0.0684(2)	0.3940(2)	
H3	0.12570	-0.05070	0.38610	0.0230
C4	0.02609(17)	0.1526(3)	0.3804(2)	
H4	-0.04020	0.09080	0.36420	0.0270
C5	0.02454(16)	0.3260(3)	0.3903(2)	
H5	-0.04300	0.38290	0.38010	0.0250
C6	0.12123(15)	0.4176(2)	0.41524(19)	
H6	0.11980	0.53690	0.42130	0.0210
C7	0.21974(15)	0.3337(2)	0.43110(18)	
N8	0.32058(13)	0.4320(2)	0.46436(17)	
H8A	0.3391(18)	0.447(3)	0.553(2)	0.0150
H8B	0.3062(18)	0.538(3)	0.423(2)	0.0150
H8C	0.372(2)	0.392(3)	0.435(2)	0.0150
N11	0.46281(13)	0.3346(2)	0.24802(16)	
O12	0.37820(12)	0.24293(16)	0.21598(15)	
O13	0.50442(12)	0.3697(2)	0.36781(14)	
O14	0.50214(12)	0.3886(2)	0.15839(15)	
N21	0.26986(14)	0.7391(2)	0.22380(18)	
O22	0.28969(17)	0.6055(2)	0.17539(18)	
O23	0.26988(13)	0.73999(16)	0.34907(15)	
O24	0.24838(12)	0.87067(19)	0.16071(16)	

Table 3: Anisotropic displacement parameters (in Å ^{2})

Atom	**U_{11}**	**U_{22}**	**U_{33}**	**U_{12}**	**U_{13}**	**U_{23}**
N1	0.0144(8)	0.0104(8)	0.0166(8)	0.0012(6)	0.0042(7)	0.0006(7)
C2	0.01400	0.01200	0.01300	0.00100	0.00500	0.00100
C3	0.02000	0.01400	0.02200	-0.00400	0.00600	-0.00400
C4	0.0173(10)	0.0264(11)	0.0233(10)	-0.0058(8)	0.0040(8)	-0.0042(9)
C5	0.0145(9)	0.0266(11)	0.0212(10)	0.0043(8)	0.0029(8)	-0.0024(9)
C6	0.0187(9)	0.0143(9)	0.0180(9)	0.0026(7)	0.0031(8)	-0.0024(8)
C7	0.0125(8)	0.0124(8)	0.0110(8)	-0.0021(7)	0.0017(7)	-0.0022(7)
N8	0.0127(7)	0.0104(7)	0.0146(8)	-0.0020(6)	0.0035(6)	-0.0019(6)
N11	0.0130(7)	0.0185(8)	0.0164(8)	0.0016(6)	0.0050(6)	-0.0014(7)
O12	0.0185(7)	0.0175(7)	0.0189(7)	-0.0062(5)	0.0042(6)	-0.0032(5)
O13	0.0175(7)	0.0413(9)	0.0131(7)	-0.0053(6)	0.0023(6)	-0.0088(6)
O14	0.0202(7)	0.0406(9)	0.0202(8)	-0.0037(6)	0.0087(6)	0.0056(7)
N21	0.0145(8)	0.0183(8)	0.0216(9)	-0.0012(6)	0.0040(7)	-0.0020(7)
O22	0.0594(12)	0.0290(9)	0.0298(9)	0.0068(8)	0.0158(9)	-0.0118(8)
O23	0.0323(8)	0.0128(7)	0.0197(7)	0.0007(6)	0.0110(6)	0.0012(5)
O24	0.0208(7)	0.0272(8)	0.0282(8)	0.0043(6)	0.0039(6)	0.0140(7)

Table 4: Selected geometric parameters (Å, °)

N1—C2	1.460(3)	C6—C7	1.387(3)
N1—H1A	0.910(24)	C6—H6	0.950(2)
N1—H1B	0.821(25)	C7—N8	1.459(3)
N1—H1C	0.902(24)	N8—H8A	0.895(20)
C2—C3	1.384(3)	N8—H8B	0.941(23)
C2—C7	1.389(2)	N8—H8C	0.853(26)
C3—C4	1.391(3)	N11—O14	1.246(3)
C3—H3	0.950(2)	N11—O13	1.245(3)
C4—C5	1.382(3)	N11—O12	1.266(3)
C4—H4	0.949(2)	N21—O24	1.225(2)
C5—C6	1.390(3)	N21—O22	1.229(3)
C5—H5	0.950(2)	N21—O23	1.302(3)
C2—N1—H1A	108.48(155)	C7—C6—C5	119.55(18)
C2—N1—H1B	114.16(187)	C7—C6—H6	120.27(16)
H1A—N1—H1B	111.43(242)	C5—C6—H6	120.18(18)
C2—N1—H1C	112.99(151)	C6—C7—C2	119.93(15)
H1A—N1—H1C	101.04(204)	C6—C7—N8	118.44(17)
H1B—N1—H1C	107.99(218)	C2—C7—N8	121.60(15)
C3—C2—C7	120.50(15)	C7—N8—H8A	106.54(146)
C3—C2—N1	118.57(17)	C7—N8—H8B	108.75(145)
C7—C2—N1	120.89(15)	H8A—N8—H8B	108.40(187)
C2—C3—C4	119.45(19)	C7—N8—H8C	115.04(174)
C2—C3—H3	120.29(16)	H8A—N8—H8C	113.83(198)
C4—C3—H3	120.26(18)	H8B—N8—H8C	104.06(213)
C5—C4—C3	120.14(20)	O14—N11—O13	121.51(16)
C5—C4—H4	119.93(23)	O14—N11—O12	118.99(16)
C3—C4—H4	119.93(21)	O13—N11—O12	119.50(16)
C4—C5—C6	120.41(20)	O24—N21—O22	123.95(17)
C4—C5—H5	119.79(23)	O24—N21—O23	118.06(17)
C6—C5—H5	119.8(2)	O22—N21—O23	117.98(17)

Symmetry code : - X, 1/2 + Y, 1/2 – Z

Table 5: Principal intermolecular distances (Å) and bond angles (°) of the hydrogen bonding scheme

D—H···*A*	*D*—H	H···*A*	*D*···*A*	*D*—H···*A*
N1—H1B···O14^{i}	0.83 (3)	2.03 (3)	2.848 (2)	172 (2)
N1—H1B···N11^{i}	0.83 (3)	2.62 (3)	3.414 (2)	160 (2)
N1—H1B···O12^{i}	0.83 (3)	2.63 (2)	3.253 (2)	133.3 (19)
N1—H1C···O23^{ii}	0.90 (3)	1.88 (3)	2.770 (2)	167 (2)
N1—H1C···N21^{ii}	0.90 (3)	2.57 (2)	3.323 (2)	141.0 (19)
N8—H8A···O12^{i}	0.89 (2)	2.22 (2)	2.875 (2)	129.6 (19)
N8—H8A···O24^{iii}	0.89 (2)	2.32 (2)	2.911 (2)	123.6 (19)
N8—H8A···O13^{iv}	0.89 (2)	2.42 (2)	2.892 (2)	113.3 (17)
N8—H8B···O23	0.94 (2)	1.79 (3)	2.724 (2)	175.6 (19)
N8—H8B···N21	0.94 (2)	2.56 (2)	3.427 (2)	154.3 (18)
N8—H8B···O22	0.94 (2)	2.58 (2)	3.230 (2)	126.7 (17)
N8—H8C···O13	0.86 (2)	1.99 (2)	2.822 (2)	163 (2)
N8—H8C···N11	0.86 (2)	2.55 (2)	3.333 (2)	152 (2)
N8—H8C···O12	0.86 (2)	2.58 (2)	3.236 (2)	134 (2)

Symmetry codes: (i) *x*, −*y*+1/2, *z*+1/2; (ii) *x*, *y*−1, *z*; (iii) *x*, −*y*+3/2, *z*+1/2; (iv) −*x*+1, −*y*+1, −*z*+1.